JOURNAL OF GEOPHYSICAL RESEARCH, VOL. 97, NO. D8, PAGES 7859–7882, MAY 30, 1992

The Structure of the Polar Vortex

MARK R. SCHOEBERL, LESLIE R. LAIT[1], PAUL A. NEWMAN, AND JOAN E. ROSENFIELD[1]

NASA Goddard Space Flight Center Greenbelt, Maryland

Reconstruction of the Airborne Antarctic Ozone Experiment and Airborne Arctic Stratosphere Expedition aircraft constituent observations, radiative heating rate computations, and trajectory calculations are used to generate comparative pictures of the 1987 southern hemisphere (SH) late winter and 1989 northern hemisphere (NH) mid-winter, lower stratospheric, polar vortices. Overall, both polar vortices define a region of highly isolated air, where the exchange of trace gases occurs principally at the vortex edge through erosional wave activity. Aircraft measurement showed that (1) between 50 and 100 mbar, horizontally stratified long-lived tracers such as N_2O are displaced downward 2-3 km on the cyclonic (poleward) side of the jet with the meridional tracer gradient sharpest at the jet core. (2) Eddy mixing rates, computed using parcel ensemble statistics, are an order of magnitude or more lower on the cyclonic side of the jet compared to those on the anticyclonic side. (3) Poleward zonal mean meridional flow on the anticyclonic side of the jet terminates in a descent zone at the jet core. Despite the similarities between the SH and NH winter vortices, there are important differences. During the aircraft campaign periods, the SH vortex jet core was located roughly $8^\circ - 10^\circ$ equatorward of its NH counterpart after pole centering. As a result of the larger size of the SH vortex, the dynamical heating associated with the jet core descent zone is displaced further from the pole. The SH polar vortex can therefore approach radiative equilibrium temperatures over a comparatively larger area than the NH vortex. The subsequent widespread formation of polar stratospheric clouds within the much colder SH vortex core gives rise to the interhemispheric differences in the reconstructed H_2O, NO_y, ClO, and O_3, species which are affected by polar stratospheric clouds.

INTRODUCTION

The polar vortex is the strong, mid-latitude, quasi-zonal, stratospheric wind system that develops during winter as a result of the latitudinal gradient in ozone heating. The purpose of this paper is to develop a comparative picture of the 1987 southern hemisphereSH and 1989 northern hemisphere (NH), lower stratospheric, polar vortex circulation and constituent distributions as observed by the Airborne Antarctic Ozone Experiment (AAOE), August 17-September 22, 1987, and Airborne Arctic Stratosphere Expedition (AASE), January 3-February 10, 1989 aircraft campaigns.

Recent numerical models of the polar vortex evolution [e.g., *Juckes and McIntyre*, 1987; *Salby et al.*, 1990] have focused on vortex interaction with forced mid-latitude planetary waves. These barotropic or equivalent barotropic models represent horizontal motions with fairly high resolution, but simplify or ignore the vertical structure. The model simulations produce a vortex that is remarkably resilient. Air on the polar or cyclonic side of the jet is isolated from mid-latitude air. As the model vortex evolves, planetary waves peel material from the outer edge of the vortex, transferring it to mid-latitudes. During this peeling or erosional process, potential vorticity and tracer gradients are sharpened producing a marked vortex boundary (e.g., an "edge").

The results obtained by the barotropic type models do not appear to be pathological. High resolution general circulation model simulations of the winter stratosphere by *Mahlman and Umcheid* [1987] show many of the same features as the barotropic-type models such as the sharpened trace gas gradients at the vortex edge. The picture of vortex edge development and subsequent erosional shrinking of the polar vortex area during winter was confirmed by *Butchart and Remsberg* [1986]. Using Limb Infrared Monitor ofthe Stratosphere satellite data, they documented the evolution of the 1979 Arctic polar vortex showing that the vortex shrinks more rapidly during winter than can be expected from pure radiative forcing alone. The accelerated erosion is due to planetary wave activity, and is particularly rapid during sudden stratospheric warmings. It is generally agreed that the lack of planetary wave activity in the SH produces a more radiatively driven vortex evolution.

Sharp edges in the long-lived tracer distributions were discovered during both AAOE and AASE missions [e.g., *Proffitt et al.*, 1989*c*; *Hartmann et al.*, 1989; *Loewenstein et al.*, 1989, 1990; *Schoeberl et al.*, 1990], confirming to some extent the vortex model predictions. Stratospheric Aerosol and Gas Experiment (SAGE II) aerosol observations [*Kent et al.*, 1985] and radioactive debris cloud data [*Telegadas*, 1967] also suggest that air within the vortex is highly isolated during winter. Nonetheless there is still some debate about the degree of isolation. The quantitative assessment of the transfer of trace gases between mid-latitudes and the vortex interior has direct implications for the interpretation of the chemical data and explanation of the ozone loss rates [*Anderson et al.*, 1989]. For example, *Hartmann et al.* [1989] concluded from the AAOE flight data that the vortex was so highly isolated from mid-latitudes that transfer of air could be totally neglected; however, *Tuck* [1989] has argued that there must be sufficient water vapor transport into the vortex from the exterior by small scale eddies to maintain Polar Stratospheric Clouds (PSCs), which were observed over the Antarctic continent into late September, 1987. Tuck also argued that the change in the vertical gradient of N_2O at the 400K potential temperature surface suggested lateral transport at least below 400K, where significant ozone destruction could occur [*Murphy*, 1991].

Proffitt et al. [1989*a*,*b*, 1990] diagnosed a circulation at

[1]Universities Space Research Association, NASA Goddard Space Flight Center, Greenbelt, Maryland.

Paper number 91JD02168.
0148–0227/92/91JD–02168$05.00

the vortex edge using the trends in the long-lived tracer, N_2O, along aircraft flight paths. By choosing an average N_2O isopleth, *Proffitt et al.* [1990] argued that since diabatic cooling occurs in the stratosphere, air parcels must move poleward along the N_2O isopleths toward the colder temperature regions. This would produce a significant circulation from the vortex exterior to the interior. Unfortunately, since average isopleths are used (which are approximately equivalent to zonal mean isopleths), Proffitt et al.'s argument neglects the eddy flux of heat (see appendix) which, to a large degree, counters the radiational cooling. *Plumb* [1990] has also pointed out that Proffitt et al.'s meridional flow is so large that it is probably inconsistent with the angular momentum budget.

Although the main goal of this paper is a comparative study of the SH and NH vortices, such a study would be incomplete without an estimate of the transport circulation. In the next section, the averaged meteorological conditions and the reconstructed constituent fields for both aircraft campaigns are compared. The reconstruction process [*Schoeberl and Lait*, 1991] allows us to produce a large-scale picture of the trace gas distributions from the in situ aircraft data. The dynamics of the polar vortex are discussed in following section, and some expected relationships between dynamical fields and long-lived trace gases are derived. A computation of the vortex mixing rates using a trajectory model is described. The derived diffusion coefficients are then applied to reconstructed constituent fields to estimate eddy fluxes. Radiative transfer computations are used to diagnose the residual circulation. Although the trajectory and radiative transfer modelling approaches are quite different they yield a consistent picture of the vortex structure and transport circulation. Our overall results are summarized and discussed in the last section.

Comparison of AAOE and AASE vortex observations

Meteorological Conditions

The meteorological data used for this study are derived from the National Meteorological Center's (NMC) analyzed stratospheric fields with potential vorticity and winds derived from the NMC temperatures and heights. The analysis procedure is described by *Newman et al.* [1988b,1989]. The NMC's analyzed stratospheric fields have been compared to the aircraft observations [*Rood et al.*, 1990]. The largest differences were are found at the coldest temperatures (~190K) where NMC analysis show a warm bias of about 2-4K. The mean difference of over the range 190K to 220K was 0.8K with a standard deviation of 1.7K. Despite the fact that the NMC analysis does not resolve small scale thermal perturbations seen in the aircraft data, the agreement between the data sets is quite good.

The AAOE SH ER-2 measurements took place during the August 17 -September 22, 1987 period. Flights with dives at the poleward terminus began August 23, but reconstruction problems were encountered using the August 23

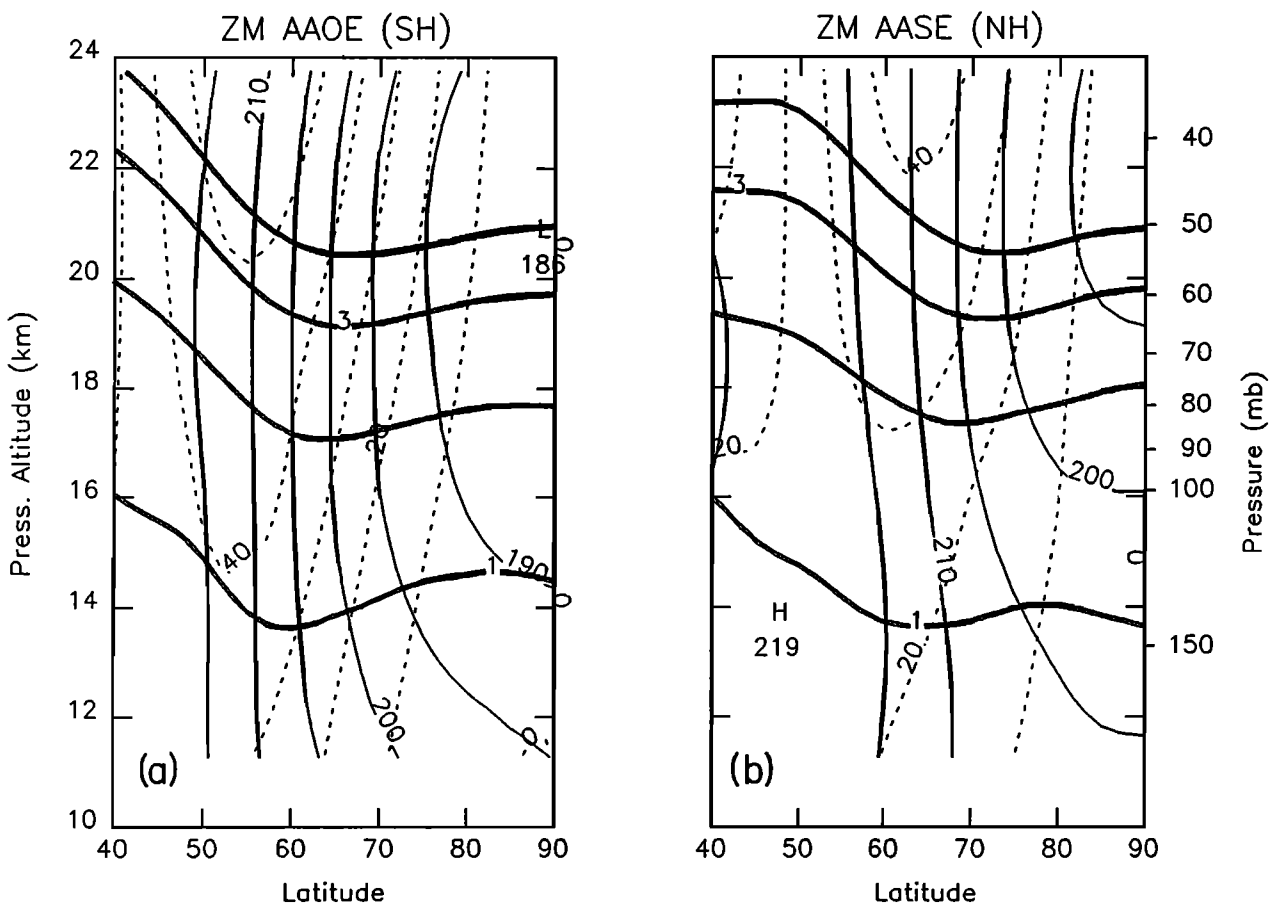

Figure 1. Potential vorticity 10^5 K m^2/kg/s (heavy solid line), zonal wind (dashed) and temperature (thin solid lines) averaged over the 1989 AASE and 1987 AAOE mission periods. (*a,b*) Zonal mean fields. (*a,b*) The same fields at 65W (10E) shifted with respect to the maximum potential vorticity gradient on the 420K (440K) isentropic surface.

data set [*Schoeberl et al.*, 1989] so the averaging period for AAOE used here begins August 28 and runs to September 22 unless otherwise indicated. A detailed description of the AAOE mission is given by *Tuck et al.* [1989]. The AASE NH ER-2 measurements took place from January 3 to February 10, 1989, and AASE is briefly summarized by *Turco et al.* [1990]. All of the data for the AASE mission were used in the analysis below, again, unless otherwise indicated.

Even though the solar zenith angles were quite different during the two mission periods, dynamically, both missions took place during a period when planetary wave activity was relatively low but beginning to increase. This is confirmed by 70 mbar vortex area analyses (not shown) which indicate little or no change in the vortex area during both the AAOE and AASE periods. However, in the southern hemisphere (SH), large wave events developed during late September, 1987 [*Newman et al.*, 1988*b*], and in the northern hemisphere (NH), a major stratospheric warming occurred just after the end of the AASE mission [*Newman et al.*, 1989]. Thus, even though both winter stratospheric periods were colder than average [*Nagatani et al.*, 1990], it can be argued that both aircraft missions sampled relatively quiescent vortices which were not atypical of winter conditions found in either hemisphere.

Figures 1a-d show the time averaged winds and temperatures for the AAOE and AASE measurement periods. Figures 1a and 1b show zonal mean fields; Figures 1*c* and 1*d* show the same fields along a fixed longitude (10E for AASE, 65W for AAOE) which approximates the longitude of most ER-2 flights. The fields in Figures 1*a* and 1*b* have been time averaged after first shifting the latitudes with respect to the maximum potential vorticity (PV) gradient at 440K (420K) for AASE (AAOE). The shift-averaging produces time-mean fields which more closely resemble the aircraft observations of steep constituent gradients across the jet.

Comparing the fields in Figures 1, it is clear that the different averaging procedures (zonal mean verses shift-averaging) make only a small difference in the SH where the vortex is usually zonally symmetric. In the NH however, the PV gradients are visibly sharper in Figure 1d compared to Figure 1b. Because the Arctic vortex generally exhibits greater zonal asymmetry, zonal averaging significantly smooths the vortex edge.

With either averaging method, it is apparent that the SH polar vortex covers a larger area, the jet axis being 8° - 10°, equatorward of the NH vortex. The Antarctic stratospheric cold temperature regions extend to comparatively lower altitudes. The interhemispheric temperature difference is, of course, the basic reason behind the appearance of the ozone hole in the SH spring. The deeper core of SH cold temperatures allows for PSC formation over a more extensive altitude range, ultimately giving rise to more complete heterogeneous chemical processing of vortex air.

Constituents

The constituent climatology shown in this section is generated using the reconstruction technique in which aircraft data are transformed into PV and potential temperature (θ) space, then reconstructed at different times and locations using meteorological analyses. Reconstruction theory is described in detail by *Schoeberl and Lait* [1991]; the reader is also referred to earlier papers by *Schoeberl et al.* [1989] and *Lait et al.* [1990]. (The basic premise for reconstruc-

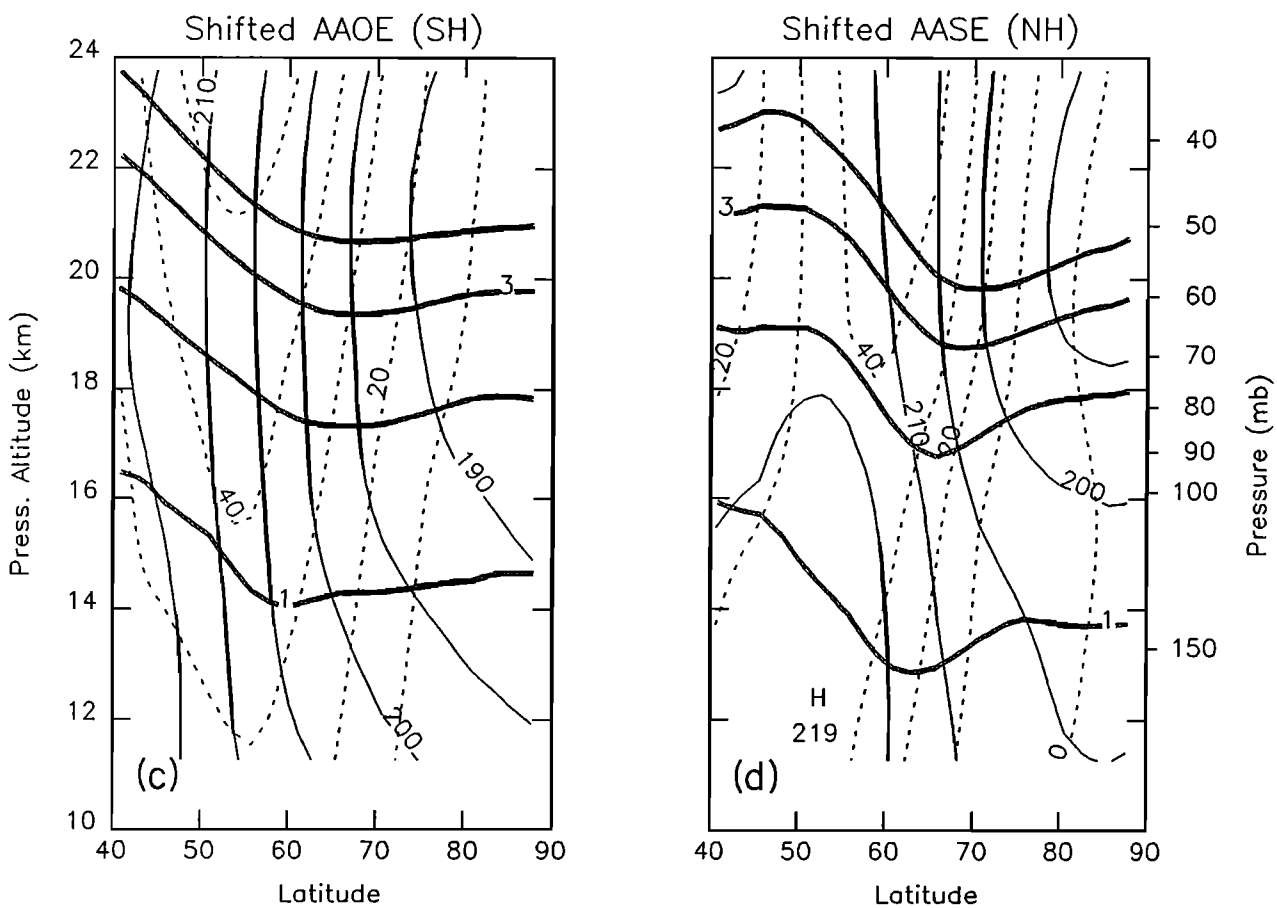

Fig. 1. (continued)

tion is that a tube of fluid bounded by two PV values and two isentropic surfaces has little constituent variation along its length. This is a good assumption for most long-lived tracers since, within the polar vortex, the strong meridional wind shear rapidly mixes constituents within a tube. However, for a chemically active species, rapid variation along the tube length can occur if the solar zenith angle varies along the tube, or if PSCs exist within some portion of the tube. The test of the reconstruction method is to generate constituent fields along the ER-2 flight path using observations from other flights (or other platforms). The generated data can then be compared to the in situ data. This kind of comparison has been performed for all of the constituents shown here with generally good results, except for the Arctic ClO observations. Although Arctic ClO reconstructions are shown, they should be considered mission averages, not very representative of individual aircraft observations.)

Reconstructions shown here are based upon ER-2 in situ data. Since the reconstructions work best for longer lifetime trace gases (t > 15 days), attention is restricted to O_3, H_2O, NO_y (after adjustment for nitrification by PSC ingestion in the NO_y data), and N_2O. ClO appeared to be better conserved during the AAOE observational period, but changed rapidly during AASE. Thus the NH ClO reconstructions are smoothed. The reconstruction algorithm takes into account linear trends in trace gases, so reconstruction of the Antarctic and Arctic fields includes, to first order, any chemical source or loss processes.

N_2O. Plate 1 shows reconstructions of the N_2O distribution for the AAOE and AASE missions using the shift-averaged fields. The corresponding meteorological data are shown in Figures 1*c* and 1*d*. Also plotted on these figures for reference are the PV and θ distributions. For both hemispheres it is apparent that the PV and N_2O distributions are highly correlated. This is not simply an artifact of the reconstruction process, but is evident in the data from individual flights [*Schoeberl et al.*, 1989].

Outside the NH vortex, Plate 1 shows a relatively flat N_2O gradient with latitude. The AAOE ferry flight data show that a similar situation exists for the SH vortex. At the edge of the vortex, which approximately corresponds to the maximum gradient in potential vorticity and the peak in the zonal wind speed (see Figure 1d), N_2O decreases rapidly toward the pole on both isentropic and pressure surfaces. The gradient in N_2O at the vortex edge is even sharper than shown in Plate 1 (e.g., *Loewenstein et al.* [1990] observed horizontal N_2O changes of 55 ppb over 3 km). In the Southern Hemisphere, almost all of the AAOE observations took place on the cyclonic side of the jet. The few flights which included extra-vortex data (e.g., the flight on August 23, 1987 shown in Figure 4 of *Schoeberl and Hartmann* [1991] show a rapid increase in N_2O on isentropic surfaces closely correlated with changes in PV across the jet axis. Thus, it is not unreasonable to suppose that the reconstructed AAOE N_2O distribution continues to follow the PV contours toward low latitudes. The distribution of N_2O shown in Plate 1 indicates that air on the cyclonic side of the vortex is displaced downward 3-4 km relative to air on the anticyclonic side. This result is quite consistent with the findings of *Kent et al.* [1985] using Stratospheric Aerosol Measurement (SAM II) data. They noted a clear 3-4 km relative subsidence of the aerosol layer at these levels within the vortex by the end of December 1979.

Poleward of the jet maximum, the AAOE and AASE reconstructions show a somewhat flatter N_2O distribution with a clear tendency for an increase in N_2O relative to pressure surfaces moving toward the pole.

Ozone. A rapid decrease in ozone took place during the AAOE observation period, thus in order to approximate the conditions within the vortex prior to the rapid chlorine catalysis of ozone, the aircraft data are averaged into an early mission period (August 28 to September 4) and a late mission period (September 4 - 22). *Proffitt et al.* [1989*b*] have argued that ozone loss is evident in the aircraft data from the earliest flights, so this "early mission" reconstruction may not be truly representative of the ozone distribution within the vortex before the ozone hole develops.

The AASE NH ozone losses were observed to be much smaller [*Schoeberl et al.*, 1990; *Browell et al.*, 1990; *Proffitt et al*, 1990]. Thus, the AASE reconstruction, which averages over the entire mission, should be fairly representative of a normal ozone distribution within the vortex.

Plate 2 shows the early mission average SH and NH ozone distribution. In the NH, O_3 like N_2O tends to follows the PV contours fairly well. In the SH however, Plate 3 shows the early mission average O_3 (unlike N_2O) tends to cross the PV contours between 55 and 75 degrees in the 14 - 18 km range. The decoupling of the ozone and N_2O–PV fields suggests that ozone loss of as much as 25% may already present in the early mission average data.

Plate 3 compares the early AAOE mission data with the late AAOE mission data. The development of the ozone hole is clearly evident poleward of 60S. An interesting tongue–like, high ozone feature centered near 60S is also visible on the right panel. The left hand side of the tongue appears to be the ozone gradient associated with the vortex boundary. Insufficient early mission data were taken in that region to show the whole feature. The right-hand side of the tongue has formed through the effect of ozone depletion.

Water. Plate 4 shows the reconstruction of the water vapor fields with the PV and temperature contours superimposed. The SH vortex shows a strongly dehydrated core which extends outward to 55 S below 375K - 400K (see Plate 1 for location of isentropic surfaces). Under normal stratospheric conditions, H_2O should behave as a long-lived tracer, and water vapor isopleths would be expected to parallel the N_2O or PV isopleths. However, since temperatures within the SH vortex are cold enough for the formation of Type II PSCs [*Kelly et al.*, 1989; *McCormick et al.*, 1989] physical removal of stratospheric water can occur. Consistent with this observation, the zone of most severe dehydration is congruent with the region of greatest ozone loss (Plate 3) and coldest temperatures.

In contrast to the SH situation, the NH vortex shows greater water concentration poleward of 65N. The isopleths of H_2O again cut across the PV contours, suggesting that H_2O inside the NH vortex has also experienced solid phase transport. The coldest Arctic vortex temperatures occur near 30 mbar [*Newman et al.*, 1989]; the Arctic vortex temperatures at 50 mbar are usually too warm to support ice PSCs. Thus if PSCs form at 30 mbar, the condensed material would fall, then evaporate, increasing the water vapor mixing ratio at lower altitudes while dehydrating the 30 mbar region. This is exactly the process suggested by the analysis of *Gandrud et al.* [1989] who correlated appearance of particles at 19 km with frost point temperatures near 22km. *Schoeberl et al.* [1990] also noted that the ER-2 profile data showed a positive trend in H_2O below 20 km, and *Wofsy et al.* [1990] have suggested a mechanism by which small ice particles coated with nitric acid trihydrate could fall several kilometers before evaporating.

NO_y. Reconstruction of NO_y was performed by first screening the data for anomalous nitrified points associated with the instrumental ingestion of particles. This screening was accomplished using the observed linear N_2O – NO_y relationship [*Fahey et al.*, 1990*b*] to eliminate any data points which significantly exceeded the predicted NO_y values. Plate 5 shows the resultant reconstruction of the

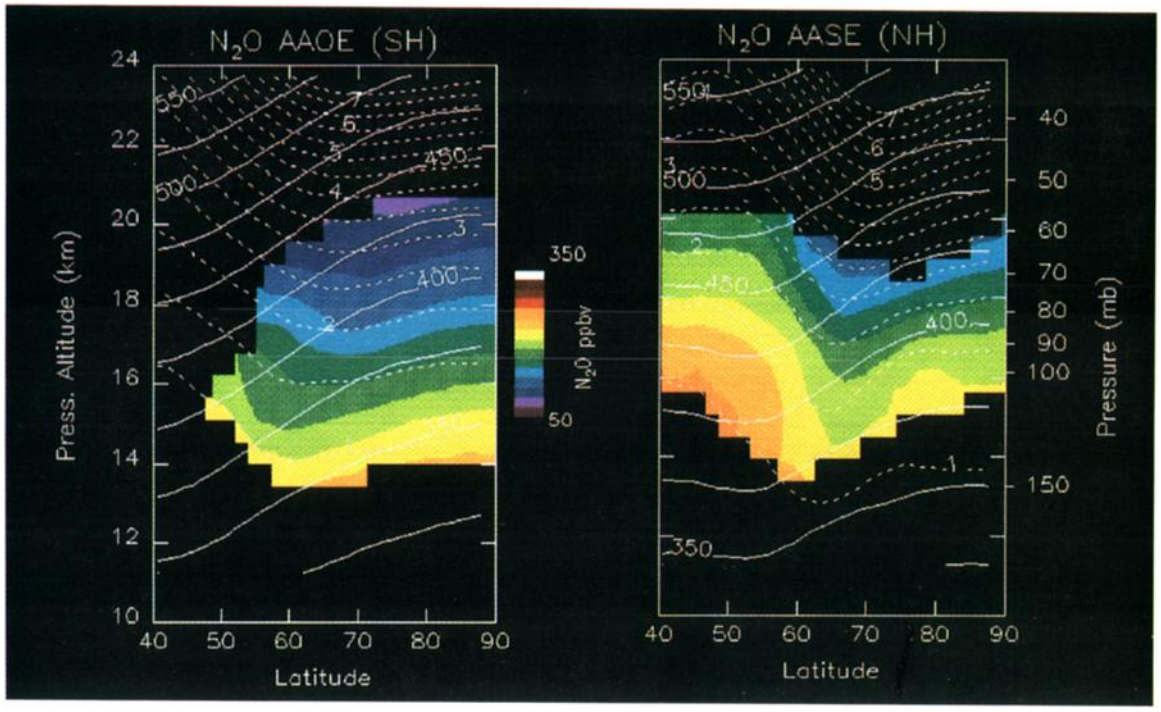

Plate 1. Reconstructions of mission-averaged N_2O for both hemispheres using the vortex shifted averages shown in Figures 1c and d. Overlaid solid lines indicate potential temperature; dashed lines, potential vorticity. (Left) SH data from AAOE, (Right) NH data from AASE. Height scale is log-pressure coordinates using a 7 km scale height; pressure values are shown on the right.

NO_y fields. The Northern Hemisphere NO_y constituent distribution tends to follow the PV contours, which is hardly surprising considering the linear N_2O – NO_y relationship mentioned above. Even though there was evidence of intense localized NO_y loss in the Arctic vortex, denitrification was not as extensive as in the Antarctic situation [*Fahey et al.*, 1990*a*]. Nevertheless, some suggestion of NO_y loss appears to be evident in the upper right-hand-side of Plate 5 where NO_y isopleths cross PV contours.

In contrast, the SH NO_y reconstruction shows evidence

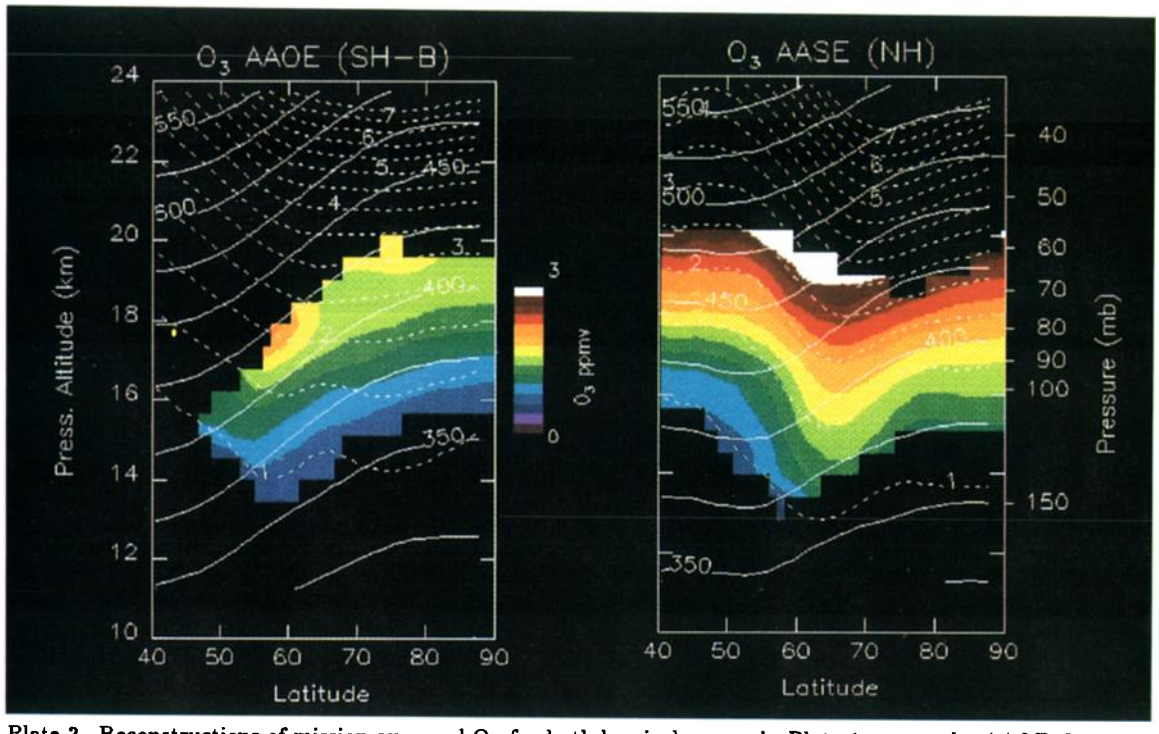

Plate 2. Reconstructions of mission averaged O_3 for both hemispheres as in Plate 1 except the AAOE data are averaged over the period August 28 - September 4, 1987 (SH–B), to approximate conditions before the development of the ozone hole.

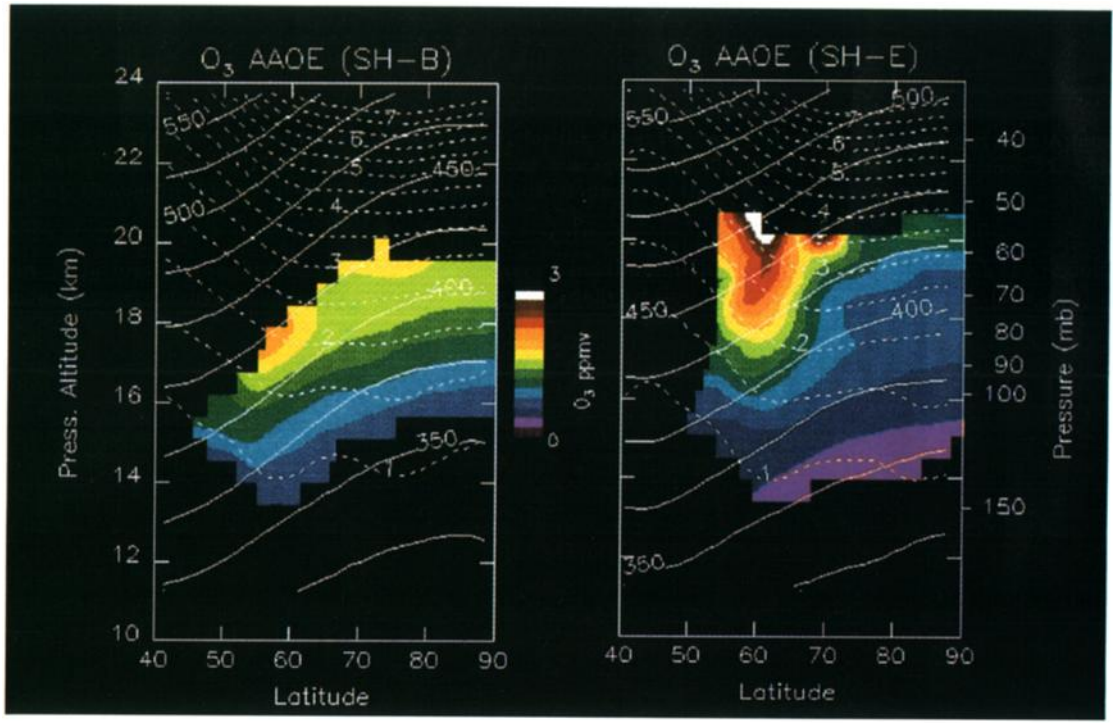

Plate 3. Two reconstructions of mission averaged O_3 for the SH as in Plate 1 (Left) Ozone averaged from August 28, 1987 - September 4, 1987 (SH-B). (Right) Ozone averaged from September 4, 1987 - September 22, 1987 (SH-E). Change in ozone poleward of 65S shows the development of the SH ozone depletion.

of significant NO_y loss in roughly the same regions where Plate 5 indicates severe dehydration. The NO_y reconstructions also show the tongue shaped feature which appeared in the ozone reconstructions for the end of the mission (Plate 3).

ClO. Plate 7 shows the reconstruction of ClO averaged over the missions. The reconstructed AAOE ClO fields show maximum ClO amounts coincident with the regions of severe dehydration (Plate 4), denitrification (Plate 5) and ozone loss (Plate 3) consistent with the current picture of the polar ozone loss mechanism [*Solomon*, 1990]. The reconstruction suggests that even higher ClO values may have occurred above the upper limit of the aircraft observations.

During the AASE mission, ClO mixing ratios increased

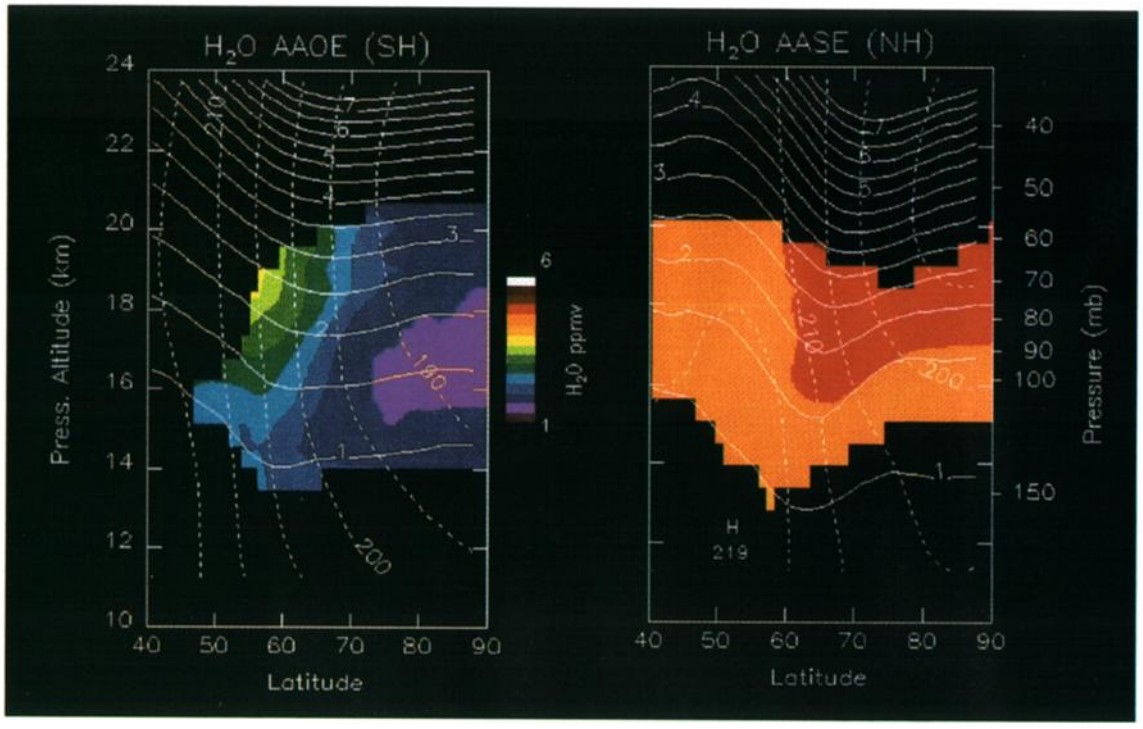

Plate 4. Reconstructions of mission-averaged H_2O for both hemispheres. Overlaid solid lines are potential vorticity, dashed lines, temperature; otherwise as in Plate 1.

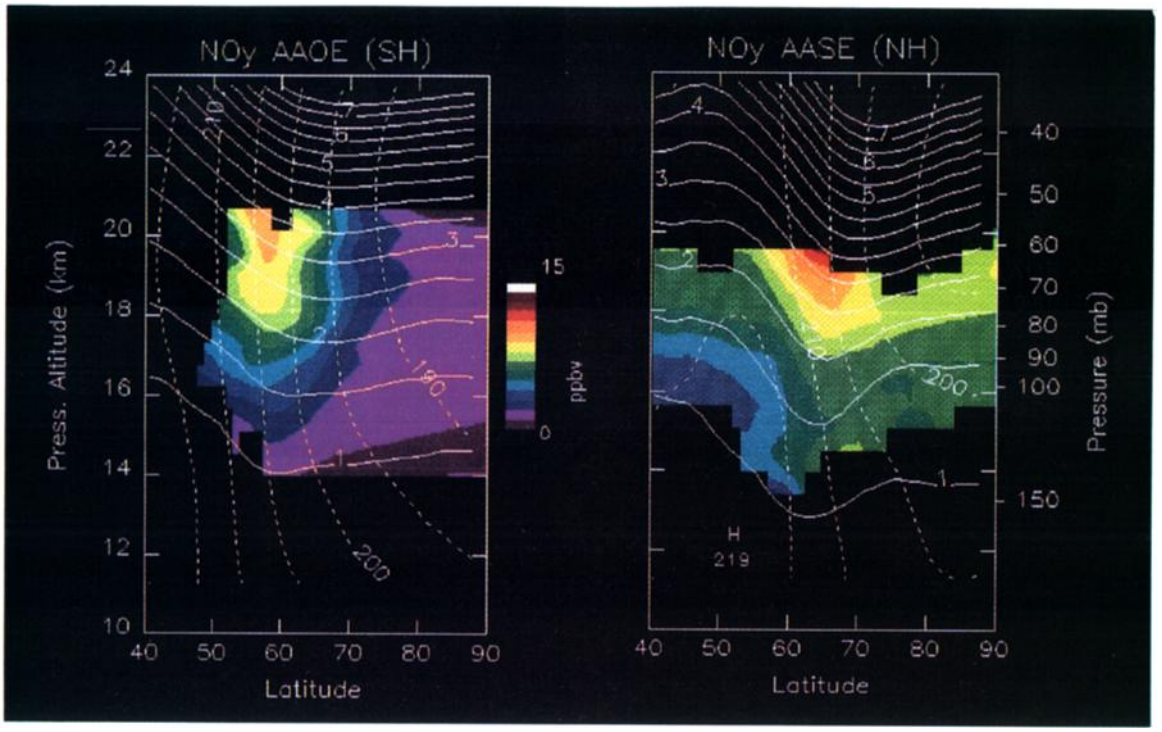

Plate 5. Reconstructions of mission-averaged NO_y for both hemispheres, as in Plate 4.

dramatically to values comparable to those observed during AAOE [*Brune et al.*, 1990]. In the time average sense, however, the ClO values were lower for AASE than AAOE which is consistent with the mission-averaged, reconstructed NH ClO. In Plate 6, the highest ClO values in the NH appear near the edge of the vortex. This is due to the effect of photolysis rather than chemistry. ClO enhancement occurs at the higher solar zenith angles on the equatorward edge of vortex [*Brune et al.*, 1990].

VORTEX DYNAMICS

As discussed above, during both AAOE and AASE campaigns, the polar vortex was fairly symmetric, and planetary wave activity was relatively weak. It is therefore appropriate to consider a zonal mean model as a first-order approximation to the vortex circulation. One of the simpler formulations is the isentropic system developed by *Galimore and Johnson* [1981] and *Tung* [1982]. This system is summarized in *Andrews et al.* [1987, pgs 142-147 and 358-361] (here-in-

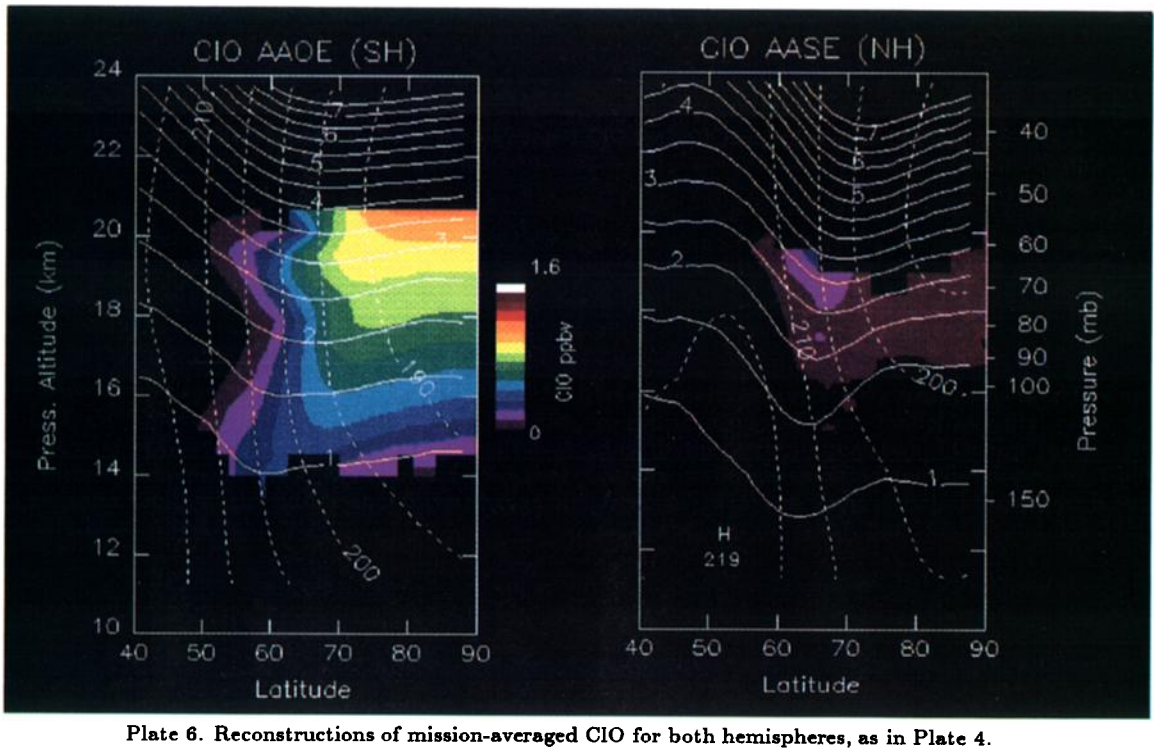

Plate 6. Reconstructions of mission-averaged ClO for both hemispheres, as in Plate 4.

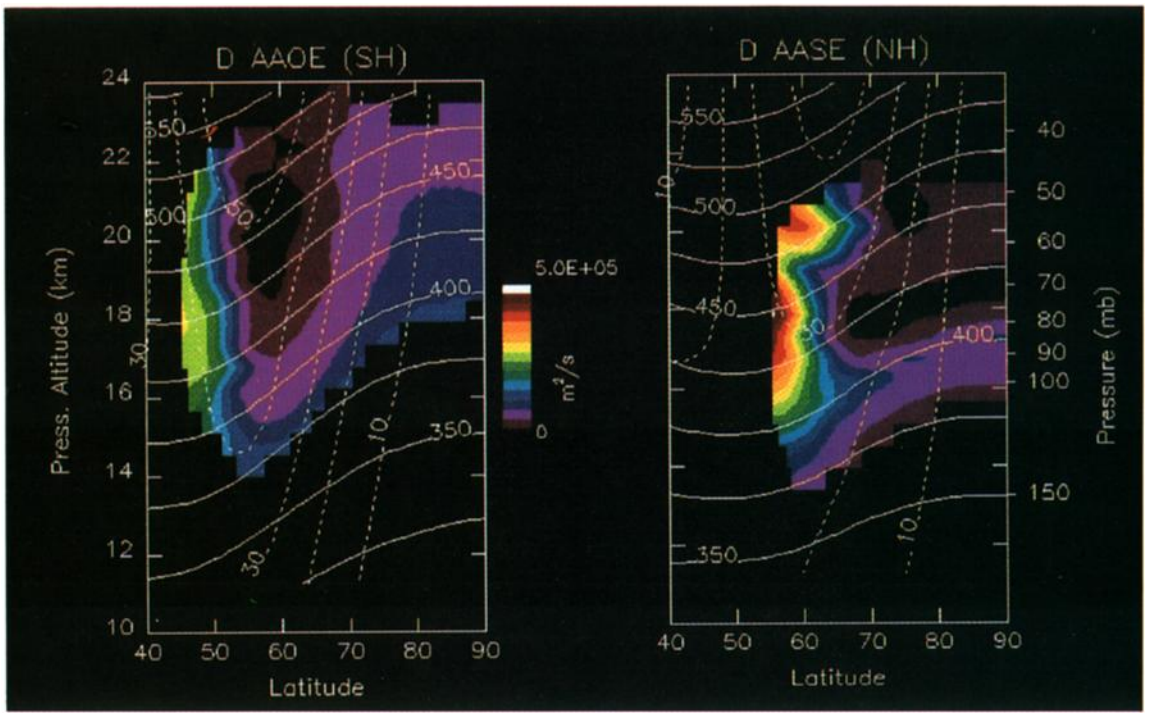

Plate 7. The isentropic diffusion rate D computed using the trajectory model for the AAOE and AASE mission periods. Overlaid is the zonal mean wind (m/s, dashed lines) and the potential temperature (K, solid lines).

after AHL). The zonal mean mixing ratio for a tracer, $\overline{\mu}$, (AHL, equation 9.4.27) is given by

$$\overline{\mu}_t + \overline{v}^* \overline{\mu}_y + \overline{Q}^* \overline{\mu}_\theta = S + (\overline{\sigma} \cos\phi)^{-1} (\overline{\sigma} D \overline{\mu}_y \cos\phi)_y \quad (1)$$

where $\overline{(A)}^* = \overline{((A)\sigma)}/\overline{\sigma}$ where A is any variable; $D = \frac{1}{2}(\overline{\eta^2})_t$; η = eddy meridional isentropic displacement, $v' = d\eta/dt$ S is the chemical source/sink; σ is the "isentropic" density, $-g^{-1}p_\theta$; $Q \equiv \dot{\theta}$, the diabatic heating rate; $y = a\phi$, where ϕ is latitude. The overbar indicates a zonal average, and the other variables have their usual meanings (see AHL).

The zonal momentum equation for this system (AHL, equation 3.9.9) is

$$\overline{u}_t - \overline{v}^* f^\dagger + \overline{Qu_\theta} = \sigma \overline{(v'P')}^* + M \quad (2)$$

where $f^\dagger = f - (\overline{u} \cos\phi)_\phi / \cos\phi$, P is Ertel's PV, the prime indicates a deviation from the zonal mean, and M is any other additional zonal acceleration not represented by the PV flux (e.g., the acceleration due to breaking gravity waves). Finally, the continuity equation is:

$$\overline{\sigma}_t + (a \cos\phi)^{-1} (\overline{\sigma}\, \overline{v}^* \cos\phi)_\phi + (\overline{\sigma}\overline{Q}^*)_\theta = 0 \quad (3)$$

Assuming quasi-adiabatic, small amplitude eddies, $P' = -\eta \overline{P}_y$. Thus the eddy PV flux may be approximated by the flux-gradient relation $\overline{(v'P')}^* \simeq -D\overline{P}_y$ [*Tung*, 1987]. Substituting into (2),

$$\overline{u}_t - \overline{v}^* f^\dagger + \overline{Qu_\theta} = -\overline{\sigma} D \overline{P}_y + M \quad (4)$$

The PV flux-gradient approximation is discussed in more detail by *Newman et al.* [1988a] and *Plumb and Mahlman* [1987]. Newman et al. point out that the use of an average D value cannot be practically justified for time scales shorter than a planetary wave life cycle (about 2 weeks). In addition, where eddy amplitudes are large, the PV flux cannot be approximated simply by the action of diffusion on a mean gradient. Because of the relatively quiet vortex, (4) and (1) should describe the conditions associated with the AAOE and AASE campaign periods.

To simplify things further, consider a quasi-steady state dynamical system in which the mean flow changes take place on a time scale much longer then the eddy mixing processes so that D does not vanish. The steady state form of (4) may also be simplified by neglecting the vertical advection of zonal momentum and M giving

$$\overline{v}^* = \overline{\sigma} D \overline{P}_y / f^\dagger \quad (5)$$

Defining the stream function solution to the steady state continuity equation (3), $\overline{Q}^* = -\psi_y/\overline{\sigma}\cos\phi$ and $\overline{v}^* = \psi_\theta/\overline{\sigma}\cos\phi$. Integrating (5) with respect to θ from an isentropic surface θ_o to infinity, where $\psi = 0$ gives

$$\psi(\theta_o) = -\int_{\theta_o}^{\infty} \overline{P}_y D f^{\dagger -1} \overline{\sigma}^2 \cos\phi\, d\theta \quad (6)$$

The downward control principal [*Haynes et al.*, 1991] can be demonstrated by differentiating (6) with respect to latitude, using the stream function relation for $\overline{Q}^*$. The result is

$$\overline{Q}^*(\theta_o) = (\overline{\sigma}_o \cos\phi)^{-1} \int_{\theta_o}^{\infty} (\overline{\sigma} D \overline{P}_y f^{\dagger -1})_y d\theta. \quad (7)$$

Thus, the diabatic heating rate, under steady state conditions, is controlled by the meridional gradient in the eddy transport of PV above the isentrope θ_o. Or the vertical transport in the lower stratosphere is determined by eddy activity in the upper stratosphere. Therefore, it is the dissipation of eddies that drives the atmosphere away from radiative equilibrium. Conversely, eddy activity (and eddy mixing) must be low in mid-latitude regions close to radiative equilibrium such as the vortex interior.

Tracer Slopes. *Holton* [1986] and *Mahlman et al.* [1986]

have presented simplified models describing the behavior of the slope of the long-lived tracer mixing ratio relative to a pressure surface. The mixing ratio for the tracer can be approximated by a global mean field which varies only with θ and a small deviation; $\overline{\mu} = \mu^o + \mu^\dagger$, where $\mu^o = f(\theta)$, $\mu^o_\theta \gg \mu^\dagger_\theta$ [*Holton*, 1980, 1986]. With these approximations, and neglecting the meridional advection of the tracer [*Holton*, 1980], (1) reduces to

$$\mu^\dagger_t + \overline{Q}^* \mu^o_\theta = S + (\overline{\sigma}\cos\phi)^{-1}(\overline{\sigma} D \mu^\dagger_y \cos\phi)_y \qquad (8)$$

Using the steady state approximation for a long-lived tracer,

$$\overline{Q}^* \mu^o_\theta = (\overline{\sigma}\cos\phi)^{-1}(\overline{\sigma} D \mu^\dagger_y \cos\phi)_y. \qquad (9)$$

Overturning by the differential diabatic heating tends to increase the meridional gradient on an isentropic surface. This overturning is balanced in steady state by the eddy mixing, which acts to weaken the gradient [*Holton*, 1986; *Hartmann et al.*, 1989].

The tracer slope relative to an isentrope, $\mathcal{S} = \tan^{-1}(\overline{\mu}_y/\overline{\mu}_\theta) \sim \tan^{-1}(\mu^\dagger_y/\mu^o_\theta)$ may now be computed. Using the definition of the stream function, (9), may be integrated with respect to latitude:

$$\mathcal{S} = \tan^{-1}\{-\psi(\overline{\sigma} D \cos\phi)^{-1}\} + \mathcal{S}_o \qquad (10)$$

where $\mathcal{S}_o$ is the tracer slope relative to θ at a boundary point on the isentrope. Thus all long-lived tracers which are principally aligned with isentropic surfaces tend have the same slope. This isentropically aligned family of tracers includes surface-emitted gases such as CH_4, N_2O, and the chlorofluorocarbons. It does not include radioactive releases or other tracers which have not approached equilibrium with the flow field.

Assuming D is independent of θ in (6),

$$\mathcal{S} = \tan^{-1}\{(\overline{\sigma})^{-1} \int_{\theta_o}^{\infty} \overline{P}_y f^{\dagger -1} \overline{\sigma}^2 d\theta\} + \mathcal{S}_o \qquad (11)$$

The fact that D vanishes from (11) simply indicates that tracer slope is not very dependent on the mixing coefficient, D, at least for the constant D case. This is not surprising since D controls both the diabatic heating through the downward control principal as well as the mixing. Thus increasing D, which tends to flatten tracer slopes, also increases $\overline{Q}^*$, which tends to steepen slopes. The effects of slope steepening and flattening through D roughly cancel. This result suggests that the interannual variability of D may not produce the same magnitude of interannual variability in the tracer slopes. Furthermore, it suggests that it may be difficult to estimate D from tracer slope information alone.

Relative tracer slopes. The relative tracer slope is the slope ($\mathcal{S}_\epsilon$) of the line on a graph where one tracer, μ, is plotted against the other, χ. This slope is given by $\mathcal{S}_\epsilon = \delta\mu/\delta\chi$ or $\nabla\mu\cdot\nabla\chi/|\nabla\chi|^2$. Since the tracers are highly stratified vertically, $|\nabla\mu| \simeq \mu^o_\theta/\cos\mathcal{S}$ and $|\nabla\chi| \simeq \chi^o_\theta/\cos\mathcal{S}$. Using these relations with (10), $\mathcal{S}_\epsilon = \mu^o_\theta/\chi^o_\theta$. Thus, for pairs of long-lived tracers plotted against one another, the relative tracer slope is the ratio of the mean vertical gradients. If both tracers are neutral then μ^o_θ is only determined by the boundary values (or fluxes) of μ^o (see AHL equation 9.7.8 with $S = 0$), and $\mathcal{S}_\epsilon$ is a straight line independent of θ (for a more general proof of this relation, see R. A. Plumb and M. Ko, Interrelationship between mixing ratios of long lived stratospheric constituents, submitted to *Journal of Geophysical Research*, 1991). However, if either tracer is chemically active compared to the transport time scale, then $\mathcal{S}_\epsilon$ will vary with θ. This result appears to explain the invariance of the slope of N_2O plotted against NO_y over a broad range of isentropic values [*Fahey et al.*, 1990*b*], since both species are long-lived tracers.

Tracer-PV Correlation. Finally, it is worth noting that provided the isentropic variation of the heating rate is small, and M can be neglected, the potential vorticity is governed by

$$P^\dagger_t + \overline{Q}^* \overline{P}^o_\theta = (\overline{\sigma}\cos\phi)^{-1}(\overline{\sigma}\cos\phi D \overline{P}_y)_y \qquad (12)$$

which has the identical form to (8) when $S = 0$. Thus PV and long-lived tracers should have roughly the same mixing slopes. In other words, a long-lived tracer such as N_2O should be highly correlated with PV as was found above (see Plate 1).

Evaluation of Eddy Diffusion Rates

From the previous section, it is clear that the transport circulation associated with the polar vortex is determined by the the magnitude of the PV flux convergence, which is effectively determined by D (6). There are two methods for estimating circulation. The first is a direct estimation of D from which $\overline{v}^*$ can be derived. The second is through a net heating rate computation which gives $\overline{Q}^*$. In this section, estimates of D are used to compute the meridional circulation.

The Diffusion Coefficient

An estimate of the value of the diffusion coefficient, D, can be made using Lagrangian trajectories of a large ensemble of parcels [*Kida*, 1983], or by examining the spread of orthogonally oriented conservative tracers [*Plumb and Mahlman*, 1987]. Here, the former approach is taken. To estimate D, 60 parcels are initialized along a PV contour. The parcel trajectories are computed for the mission periods, and the growth of the ensemble average parcel displacements are used to estimate D.

The Trajectory Model. The trajectory model is based upon the standard isentropic formulation [e.g., *Austin and Tuck*, 1985] using balanced winds derived from NMC 1200 GMT analyzed heights and temperatures to advect the parcels. The stratospheric winds are linearly interpolated in time and space to parcel positions. The trajectory model has been tested for numerical error by running it forward and backward for a set of sample trajectories over 10-day periods. The accumulated 10 day error is usually less than a degree in longitude.

In the absence of diabatic processes, parcels following an isentropic surface must also conserve PV. Thus the accuracy of a trajectory can be checked by interpolating PV to the particle path. This check was performed for each trajectory computation, and the overall degree of PV conservation was also found to be quite good.

Diffusion Computations. The diffusion rate D is $\frac{1}{2}(\overline{\eta^2})_t$, where the displacement η is the meridional deviation of the air parcel from the zonal mean position. To approximate the zonal mean system, a large number of parcels are used, and zonal averaging is replaced by ensemble averaging. The parcel displacement η is redefined as the displacement relative to the ensemble average; $\eta_i = y_i - < y_i >$, where y_i is the latitude position of parcel i and the angle brackets denote an ensemble average. The change in the position of the ensemble average is the Lagrangian mean velocity; however, that velocity has no physical meaning if balanced winds are used. With these definitions,

$$D = \frac{1}{2} < \eta_i^2 >_t \qquad (13)$$

If a zonal ring of parcels are initialized along a latitude cir-

cle, and the flow is not zonally symmetric, rapid parcel dispersal takes place as each individual parcel moves to follow separate PV contours. The relative displacements increase rapidly, then usually equilibrate as parcels settle into different "orbits" in the vortex. The initial adjustment period produces a spuriously high value for D, not appropriate for evaluating the mixing rate of long-lived tracers in near equilibrium with the flow field. Alternatively, a ring of parcels can be initialized along a PV contour. This method produces no initial rapid parcel dispersal and is consistent with the PV conservation properties of the parcels.

Table 1 shows the PV and θ values used to initialize parcel trajectories for AAOE and AASE diffusion computations. In both cases, 60 parcels are used along each contour. Tests were run using twice as many parcels to check the statistical robustness of the results, and negligible differences were found.

Figure 2 shows the change in the average squared displacement, and day to day values of $< \eta_i^2 >_t$ for a typical trajectory computation. Note that the average squared displacement exhibits transient fluctuations on the daily time scale; however, these fluctuations are largely reversible. Superimposed upon the higher frequency changes is a systematic overall increase in the average squared displacement. It is this systematic increase in mean parcel displacements which is the overall "diffusive" transport.

Two methods of evaluating the time derivative in (13) are used. In the first method, the linear tendency of $< \eta_i^2 >$ is used to calculate D. The linear fit is shown in the upper part of Figure 2, and the diffusion rate computed using the tendency is given in the figure.

The second method of evaluating D involves a finite difference computation of $< \eta_i^2 >_t$ at each trajectory time step (0.02 days), and an average of D over the time period is shown. The value of D obtained using this method is shown in the bottom panel of Figure 2. Both methods usually yield very similar results as Figure 2 indicates.

Validation of the diffusion rates from the trajectory computations is difficult. Errors associated with the estimation of D can arise from a variety of sources. First, the trajectories are only as good as the analyzed fields. The ER-2 measured winds have been compared to the balanced winds computed from NMC analysis. The rms difference ranges from 2 to 5 m/s, some of which is due to gravity waves not present in the lower resolution NMC analysis.

A second source of error is the trajectory finite difference scheme. Both analyzed wind and finite difference errors, if random, should be minimized by ensemble averaging; however, the positional errors due to wind or difference scheme errors can be cumulative, giving rise to a spurious dispersion of parcels. Thus D computed by the trajectory method should be considered an upper bound as far as numerical and wind error is concerned. For this reason, the larger value resulting from the two methods for computing D is always used.

Still unresolved is the question of how systematic uncertainty in the wind field may relate to estimates of the dispersion rate. If the data were perfect, and all scales of motion were represented, then true ensemble dispersion would result only from transience and dissipation of Rossby and gravity waves, molecular diffusion and turbulence. The latter two processes act over such small scales that they can, in effect, be ignored for the lower stratosphere unless small parcel mixing is being considered [*Prather and Jaffe*, 1990].

Synoptic and mesoscale Rossby wave systems, penetrating from the troposphere, are generally evanescent in altitude. They are probably not strongly damped radiatively. Unfortunately, these systems cannot always be adequately represented by the $5^\circ \times 2.5^\circ$ NMC grid. It can, therefore, be argued that their presence contributes "noise" to the background wind field, producing additional ensemble dispersion. Nonetheless, a situation can still be imagined where the gridding process "smooths" the synoptic field and actually reduces the variance in the wind. However, recall that it is the change in the ensemble averaged squared displacement that determines D, so that even systematically smoothed fields may have a small impact if the diffusion is primarily driven by changes in larger scale waves. If the poorly resolved scales of motion were significantly contributing to D in a systematic fashion, then individual parcel PV conservation would be visibly influenced. From an examination of the PV conservation data, there is no apparent evidence that the poorly resolved scales are having such an effect.

Gravity waves, unless breaking, tend to produce short-term, mostly reversible changes in the flow field. The mixing associated with breaking gravity waves tends to be cross isentropic rather than meridional, and no horizontal PV transport is involved. Thus breaking gravity waves cannot contribute to D in a strict sense, but their influence could be felt as an overall forcing of the zonal mean flow. In any event, gravity wave breaking is not considered to be a significant source of mixing in the lower stratospheric polar region [*Fritts*, 1984].

To summarize, it is difficult to truly validate the ensemble trajectory computations of D. Arguments given above suggest that the trajectory estimates of D are probably upper bounds. Further validation evidence will be presented below.

Overall Diffusion Rate. Since the D coefficients are as-

TABLE 1. Southern Hemisphere Computed Mixing Coefficients at PV and θ Locations

θ	PV x 10^5m^{2}K/kg/s	Diffusion Coef., D, (m^2/s)
400.	-1.1	1.2E+05
	-1.5	1.5E+05
420.	-1.1	1.8E+05
	-1.5	8.3E+04
	-2.0	6.7E+04
440.	-1.1	2.5E+05
	-1.5	7.5E+04
	-2.0	6.5E+04
	-2.5	6.8E+04
	-3.0	8.2E+04
460.	-1.5	3.2E+05
	-2.0	2.8E+04
	-2.5	3.2E+04
	-3.0	4.0E+04
	-4.0	9.2E+04
480.	-2.0	2.5E+05
	-2.5	1.4E+04
	-3.0	1.5E+04
	-4.0	4.0E+04
	-5.0	8.3E+04
500.	-2.0	3.0E+05
	-2.5	1.4E+05
	-3.0	1.3E+04
	-4.0	7.1E+03
	-5.0	3.7E+04
	-6.0	9.3E+04
520.	-3.0	1.1E+05
	-4.0	2.6E+03
	-5.0	3.1E+04
	-6.0	2.5E+04
	-8.0	7.5E+04
540.	-3.0	3.2E+05
	-4.0	4.6E+04
	-5.0	3.5E+04
	-6.0	3.3E+04
	-8.0	3.1E+04

Read 1.2E+05 as 1.2×10^5, for example.

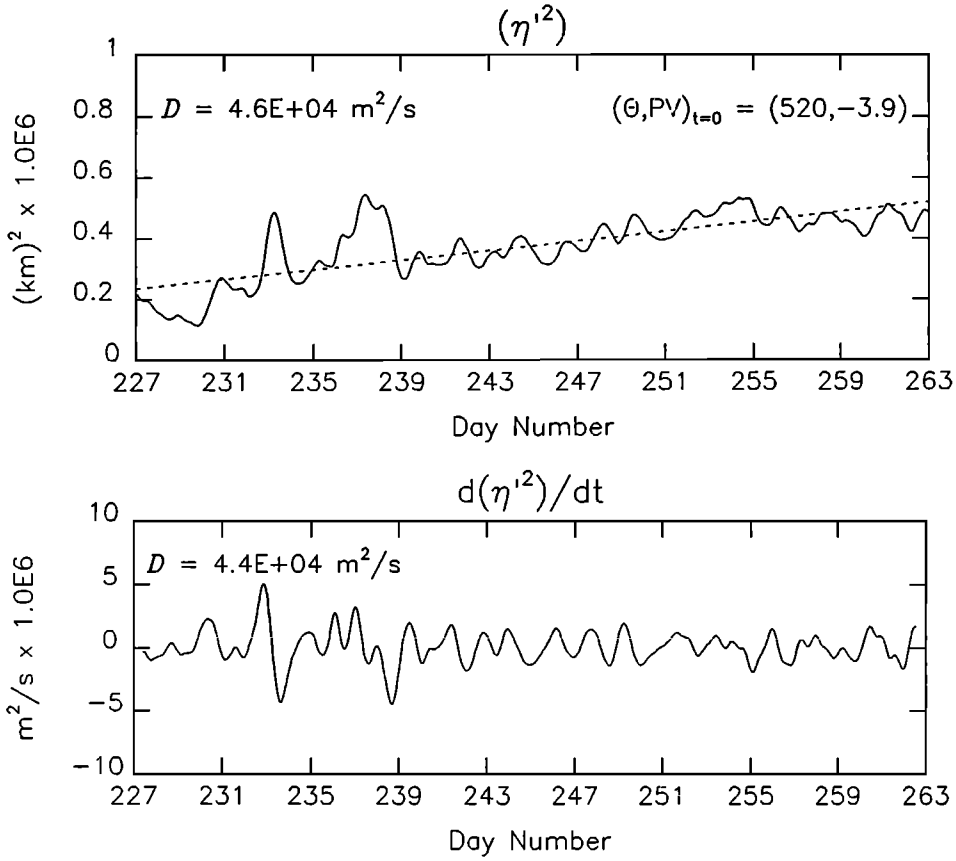

Figure 2. The ensemble-averaged squared displacement for 60 parcels as a function of time (upper panel). These parcels were initialized approximately along the $-4.0\text{x}10^{-5}\text{m}^2/\text{kg/s}$ PV contour on the 520K isentropic surface (solid line, upper panel). The actual ensemble average PV is $-3.9\text{x}10^{-5}$. The dashed line shows the linear fit from which the tendency is computed in the evaluation of the diffusion rate D given in the panel. The lower panel shows the instantaneous tendency for the ensemble average squared displacement. The average of the instantaneous tendency is used to compute D given in the lower panel.

signed to θ and PV values, the reconstructive mapping from (θ, PV) space can be used to map the structure of the D relative to the vortex. Plate 7 shows D for both hemispheres using the values from Tables 1 and 2. In both hemispheres, the mixing rates on the cyclonic side of the vortex are small.

TABLE 2. Northern Hemisphere Computed Mixing Coefficients at PV and θ Locations.

θ	PV x 10^5m^{2}K/kg/s	Diffusion Coef., D, (m^2/s)
400.	1.0	8.8E+04
	1.2	4.2E+04
420.	1.2	8.4E+04
	1.5	7.3E+04
	2.0	7.3E+04
440.	1.3	3.5E+05
	1.5	2.4E+05
	2.0	1.9E+04
	2.5	1.9E+04
460.	1.8	4.0E+05
	2.0	4.0E+04
	2.5	6.8E+03
	3.0	6.6E+04
480.	2.0	5.7E+05
	2.5	5.0E+04
	3.0	6.4E+04
	4.0	1.1E+04
500.	2.5	2.4E+05
	3.0	4.4E+05
	4.0	6.2E+04
	5.0	2.0E+04

between 10^4 and 10^5 m^2/s. Note that the mixing value of $4.0\text{x}10^4$ m^2/s implies a diffusion time of 1 year over a 1000 km length scale. Thus material inside the vortex is highly isolated even from nearby inner vortex regions. This result is consistent with the observation by *Schoeberl and Hartmann* [1991] that the sharp "edge" in chlorine monoxide was well within the Antarctic vortex boundary. The maintenance of an edge in ClO and NO_y during the AAOE mission period requires extremely low mixing rates [*Hartmann et al.*, 1989]. Plate 7 also shows that D increases towards lower altitudes in the Antarctic, rising by almost an order of magnitude from 480K to 400K. This result appears to be in agreement with the suggestion made by *Tuck* [1989] that mixing along isentropes at and below 400K is greater than above.

Moving to the equatorward (anticyclonic) side of the NH and SH jets, D values rise sharply. The magnitude of D in the mid-latitude region is consistent with estimates made by *Newman et al.* [1988*a*] and *Yang et al.* [1990]. The overall results are qualitatively consistent with the high resolution barotropic-type models [*Juckes and McIntyre*, 1987] which show mid-latitude eddies rapidly dispersing material eroded from the vortex.

Circulation. The computed diffusion rates can be used to estimate the steady state meridional isentropic circulation (5) from the eddy flux of PV. Plate 8 shows the zonal mean acceleration associated with the eddy PV flux ($\overline{\sigma} D \overline{P}_y$), and the meridional circulation (assuming a steady state). PV transport produces significant deceleration on the anticyclonic side of the jet in both hemispheres, with a correspond-

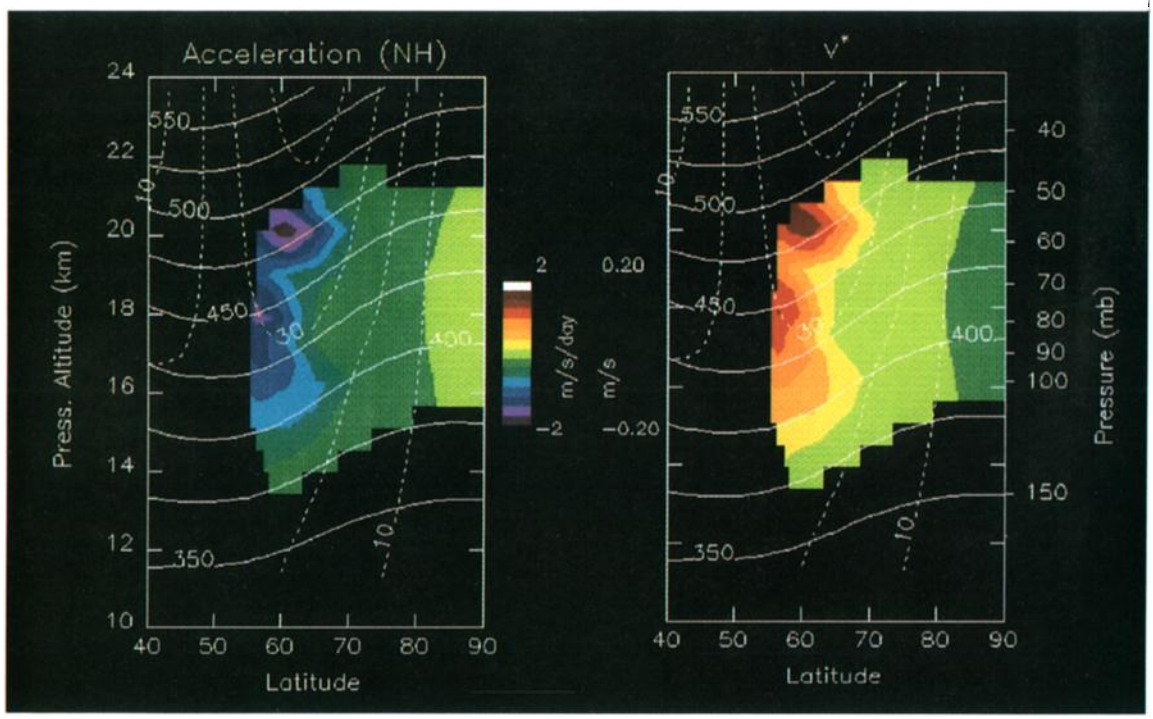

Plate 8. The acceleration and meridional circulation associated with the eddy PV flux computed from $\overline{\sigma} D \overline{P}_y$. The acceleration is in m/s/d; $\overline{v}^*$ is in m/s. (Note that poleward meridional flow in the Southern Hemisphere will produce negative values for $\overline{v}^*$.) (*a*) NH AASE period ; (*b*) SH AAOE period. Overlays as in Plate 7.

ing poleward transport by the meridional circulation. On the cyclonic side of the jet, the deceleration and poleward flow are much weaker, falling to negligible values.

The deceleration in Plate 8 is located in a region consistent with the picture of eddy erosion of the vortex edge. The strong poleward gradient in $\overline{v}^*$ suggests that significant vertical motion must occur at the vortex edge. Since the $\overline{v}^*$ field is about twice as large in the NH, the radiative heating region, $\overline{Q}^*$, may be equivalently larger or cover a broader area.

Tracer Fluxes

The reconstructed constituent distributions can be used with the isentropic diffusion coefficients to evaluate isen-

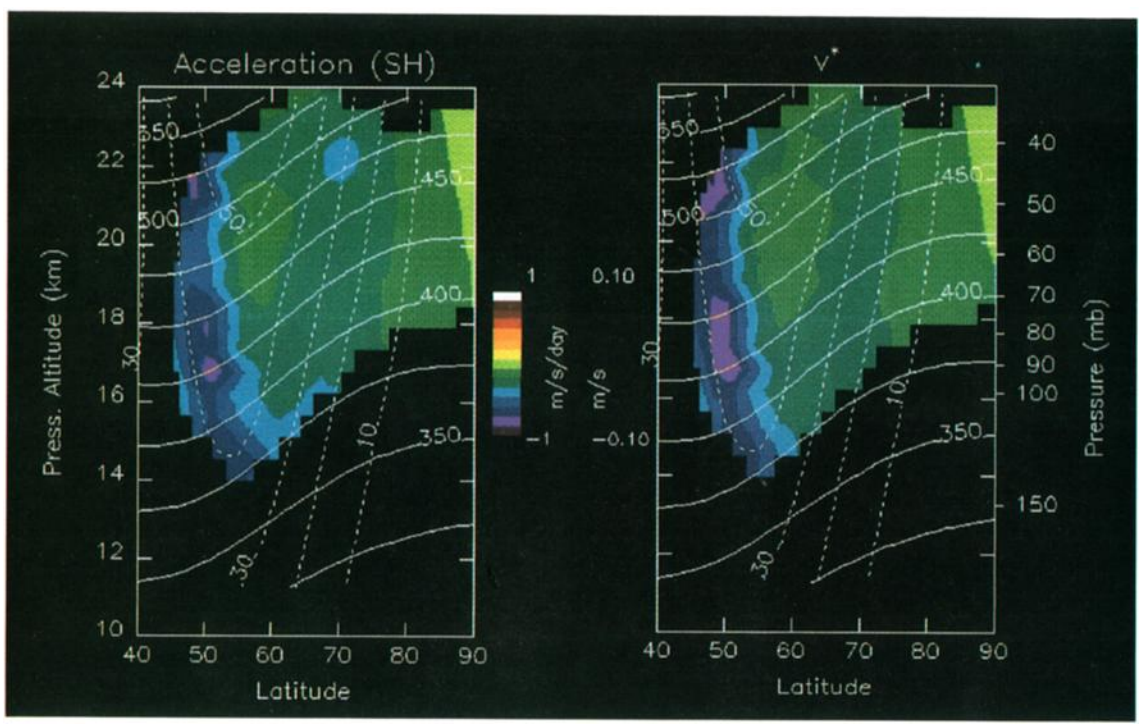

Plate 8*b*

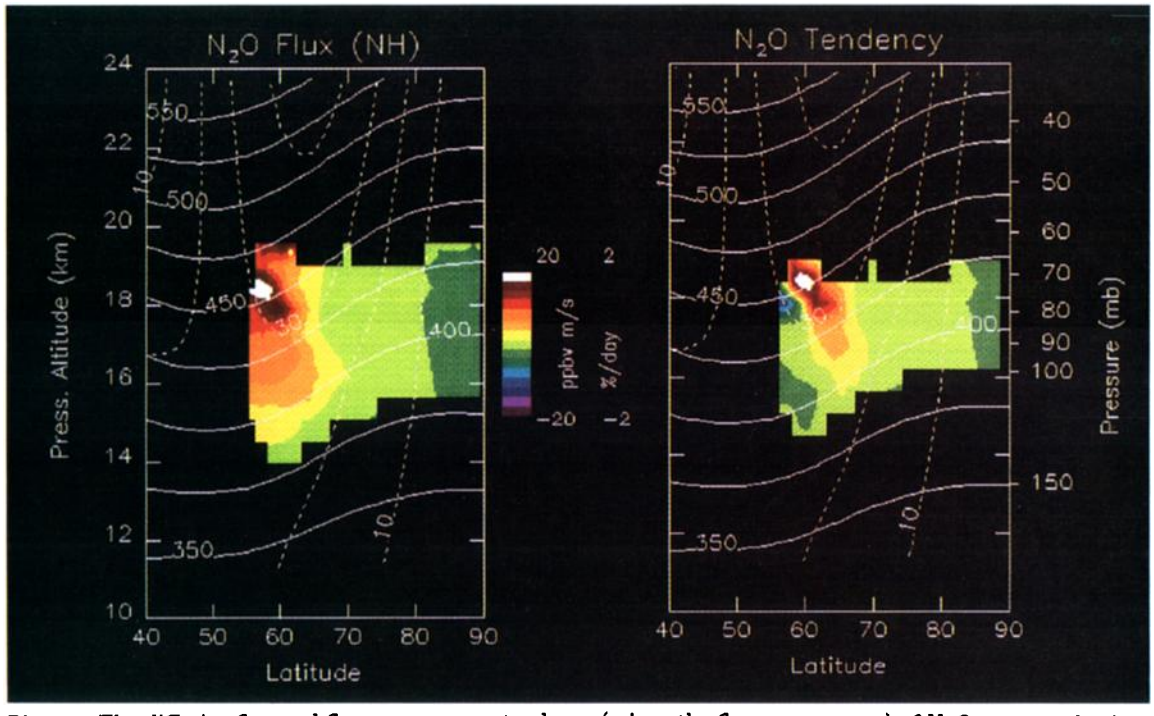

Plate 9. The diffusive flux and flux convergency tendency (minus the flux convergence) of N_2O computed using the reconstructed constituent fields (Plate 1) and diffusion coefficients (Plate 7). Overlays as in Plate 7; (*a*) NH, (*b*) SH.

tropic tracer fluxes and the tendency associated with the diffusive flux convergence (see (8)). The assumption in this calculation is that the PV flux-gradient relation is also a valid approximation for tracer flux estimates. Since the flux-gradient relation produces reasonable results in the circulation computations, there is no reason to believe that the flux-gradient approximation would not be valid for tracer transport.

Because the diffusion coefficients are computed for a zonal mean system, the constituent reconstruction is done using the zonally averaged PV and θ fields (Figures 1c and 1d). Direct computation of the diffusive flux convergence tends to produce somewhat noisy fields, so fluxes and tendencies smoothed over 5° latitude intervals along the 420 ± 5K contour are also computed. The averaged fluxes and tendencies are given in Table 3.

N_2O. Plate 9 shows the computed N_2O fluxes and the eddy flux tendency (the negative eddy flux convergence) for

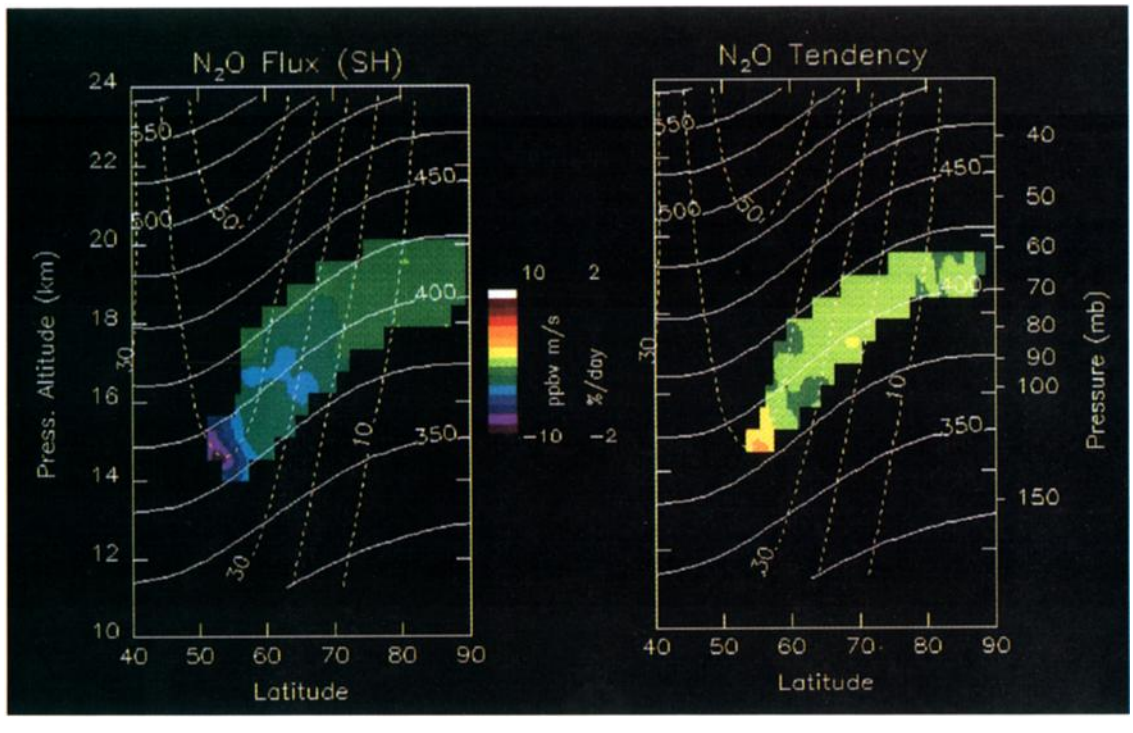

Plate 9*b*

TABLE 3. Eddy Constituent Fluxes and Flux Tendencies $\theta = 420K \pm 5K$ (~19 km)

	Latitude					
	55	60	65	70	75	80
	Northern Hemisphere (AASE)					
N_2O flux, ppbv m/s	5.	7.	5.	1.	0.3	2.4E-2
N_2O Tendency %/d		6.7E-2	0.2	0.2	7.6E-2	2.0E-2
O_3 flux, ppmv m/s	-0.1	-0.1	-7.0E-2	-1.2E-2	-3.5E-3	-2.7E-4
O_3 tendency, %/d		-0.4	-0.6	-0.3	-5.6E-2	-2.0E-2
	Southern Hemisphere (AAOE)					
N_2O flux, ppbv m/s	-3.	-2.	-3.	-1.	-0.4	-0.1
N_2O tendency, %/d	0.2	7.7E-2	6.6E-2	0.2	9.7E-2	2.3E-2
O_3 flux, ppmv m/s (Sept. 4-22)	2.3E-2	-1.2E-2	-1.0E-2	-1.7E-2	-6.5E-3	5.3E-4
O_3 tendency, %/d (Sept. 4-22)	-0.3	-0.3	3.0E-3	6.2E-2	0.2	0.1
H_2O flux, ppmv m/s	1.6E-2	-4.1E-2	-6.2E-2	-3.4E-2	-1.4E-2	-4.8E-3
H_2O tendency, %/d	-3.9E-2	-0.2	6.9E-2	0.2	0.2	8.3E-2
ClO flux, ppbv m/s	-5.4E-3	-8.9E-3	-9.6E-3	-3.2E-3	4.1E-4	2.4E-4
ClO Tendency, %/d	-0.4	9.2E-2	-0.2	-0.4	-0.2	-9.9E-2

both hemispheres. In the Northern Hemisphere, the largest region of N_2O flux is at the edge of the vortex, where relatively high amounts of N_2O on the anticyclonic side of the jet are being "diffusively transported" toward the pole and increasing the N_2O tendency on the poleward side of the maximum flux region. The effect of the N_2O flux is thus to fill in the low N_2O polar region. Note that the tendency is only significant at the edge of the vortex, consistent with the idea that most of the constituent changes are taking place at the vortex edge.

By comparison with the Arctic, the poleward flux of N_2O in the Antarctic is very weak even near 400K, where D is comparatively larger relative to the levels above (Plate 7). Near the core of SH jet, the N_2O tendency is larger, but it is still below the magnitude computed for the Arctic. Table 3 shows that on the cyclonic side of both vortices, the N_2O diffusive flux tendency is computed to be less that 0.2%/d.

Ozone. The fluxes and tendencies for ozone are shown in Plate 10. For AASE, the calculation averages over the entire mission period, but for AAOE the computation uses the end of the mission reconstruction shown in Plate 3, right. For the NH vortex (Plate 10*a*), the ozone fluxes and tendency are similar (except oppositely signed) to those found for N_2O. This is not an unexpected result considering the similarity in the N_2O and O_3 reconstructions. As with N_2O, the eddy tendencies are very small; Table 3 shows tendencies of less than 0.3%/d poleward of 60N. This is comparable to the N_2O tendency in the same region (0.2%/day). Any chemical O_3 loss on the 420K surface would therefore have to exceed a dynamical tendency of ~0.2%/d to be statistically detectable. *Schoeberl et al.* [1990] reported that the ozone loss during the AASE mission was 0.44%/d with a 0.3%/d 95% confidence limit error. Those computations appear to be consistent with the above estimates.

As discussed in the introduction, a remaining question concerning Antarctic ozone loss is the magnitude of eddy ozone flux into the chemically depleted region from outside the ozone hole. To estimate this flux, the reconstructed fields from the end of the AAOE observation period are used, since the ozone depletion is clearly evident in Plate 3. The AAOE in situ ozone decrease was observed to be about 1.0-2.0%/d [*Hartmann et al.*, 1989]. Plate 10*b* shows a poleward eddy flux of ozone at the edge of the ozone hole region, and a subsequent positive O_3 tendency near 65S at 400K. This tendency varies between 0 and 1.2 %/d; however, the average eddy tendency (Table 3) is about 0.2%/d or, over the mission period, about 15% of the observed ozone loss. This estimate agrees with calculations by *Hartmann et al.* [1989]. They computed a dynamical O_3 tendency of 20% ± 10% of the photochemical sink. Thus these computations suggest that eddy transport of ozone can be neglected as a zeroth order contribution to the photochemical loss as argued by *Anderson et al.* [1989].

Water. Because of the weak gradients in the NH reconstructed H_2O (Plate 4), fluxes and tendencies are computed only for the SH. Plate 11 shows a poleward flux of water between 60S and 70S. This flux produces dehydration in the 55-62S region with hydration closer to the pole. The hydration rates average 0.2%/d (Table 3) even though Plate 11 shows values as high as 0.8%/d in limited areas.

As previously mentioned, poleward of 65S, stratospheric temperatures frequently reach frost point or below. Subsequent PSC formation and particle settling dehydrate the air. PSC dehydration will be offset by water vapor flux from the less dehydrated region between 55 and 65S. If the eddy hydration rate is balancing the 65S-pole PSC loss, then the region between 55 and 65S (which has approximately the same area at the 65S-pole region) is dehydrating at the same rate through eddy transport of dry polar air northward. The air in the 55-65S region has a mixing ratio of 2-3 ppmv (Plate 4), about 50% lower than extra-vortex Arctic air or LIMS SH water vapor estimates [*Remsberg et al.*, 1984]. At a dehydration rate of 0.2%/d, it would require 250 days to produce the low water vapor mixing ratios present in the 55-65S region by eddy transport. Thus it does not seem possible for eddy mixing to be responsible for the dehydration in the 55-65S region as argued by *Tuck* [1989], unless the mixing rates were substantially higher in the winter months prior to the mission. A more reasonable alternative explanation is that PSC dehydration also occurs albeit intermittently in the 55 and 65S region as well. An examination of NMC analyzed temperatures indicates that ice particle formation temperatures were reached in the 55-65S region for brief periods during late July 1987.

ClO. Plate 12 shows the SH ClO flux and tendency; Northern hemisphere values are not computed because of the high variance in the reconstructed fields. As a result of the large gradient in ClO (Plate 6), there is a significant equatorward flux, $\sim 1.0 \times 10^{-2}$ ppbv m/s. This produces a strong flux convergence of 0.4%/d into the 55-65S area of the vortex. Since the NO_y mixing ratios are higher at those latitudes, ClO transported into that part of the vortex would be quickly converted to chlorine nitrate, $ClONO_2$. *Toon et al.* [1989] infer a large column abundance in $ClONO_2$ equatorward of the high ClO region, consistent with this result. However, it is not clear if the excess $ClONO_2$ observed by Toon et al. is only due to transport; $ClONO_2$ may also be enhanced during the intermittent July PSC events as discussed above. In any event, the high chlorine nitrate measurements are consistent with ER-2 measured levels of ClO and NO_y as discussed by *Kawa et al.* [this issue].

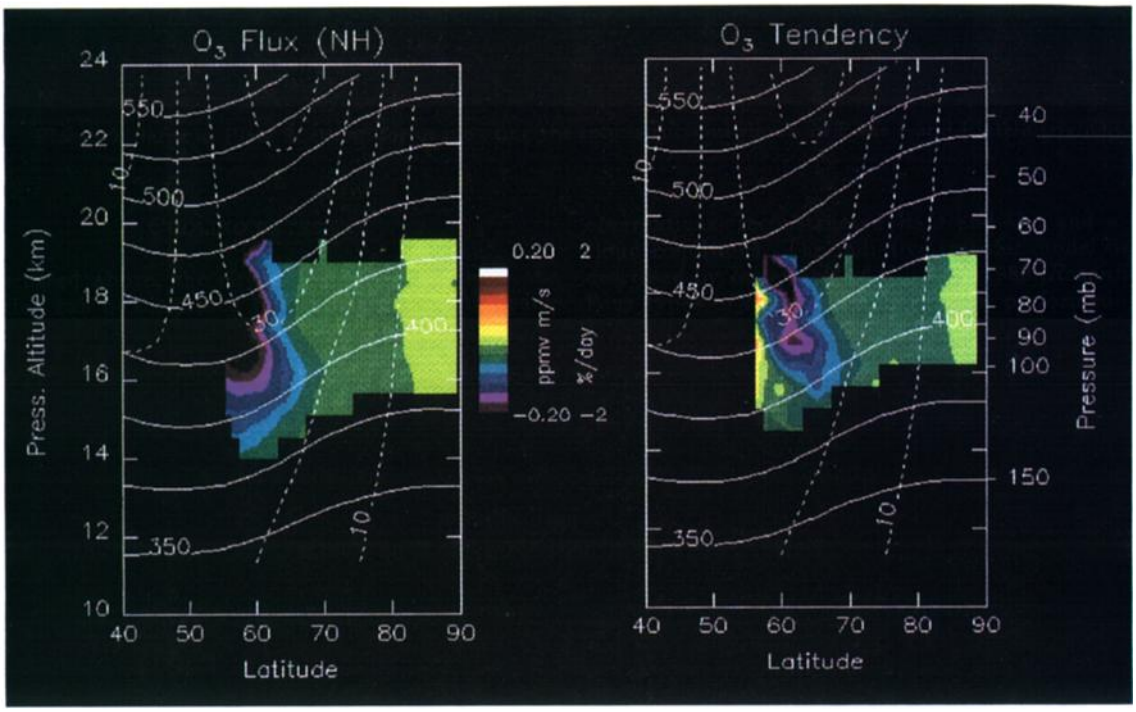

Plate 10. Same as Plate 9, except for ozone using the reconstructions shown in Plate 2 and Plate 3 (right).

COOLING RATES

As discussed above, the circulation associated with the polar vortex can be diagnosed by computation of the eddy PV transport or by computing the net radiative heating. Computation of the net heating rates provides an important check on the magnitude of the meridional flow computed in the last section. Net radiative cooling rates have been calculated for each mission day using the NMC temperature observations, reconstructed H_2O and O_3, and a variety of cloud conditions. The radiative transfer model used is that described by *Rosenfield et al.* [1987; 1989]; *Rosenfield* [1991]. Four types of calculations have been performed: clear sky conditions, tropospheric clouds, clear skies with PSCs in the stratosphere, and PSCs in the stratosphere with tropospheric clouds. The companion paper by *Rosenfield* [this issue] describes the PSC generation algorithm and the specification of the tropospheric clouds. The four cases are de-

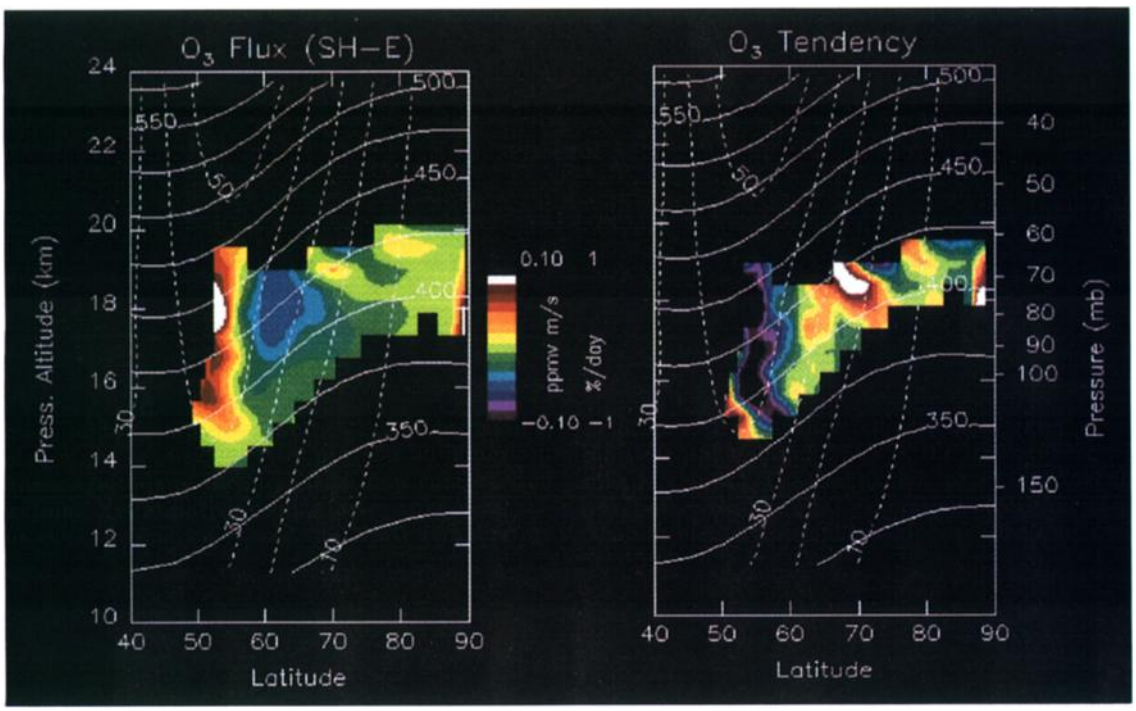

Plate 10*b*

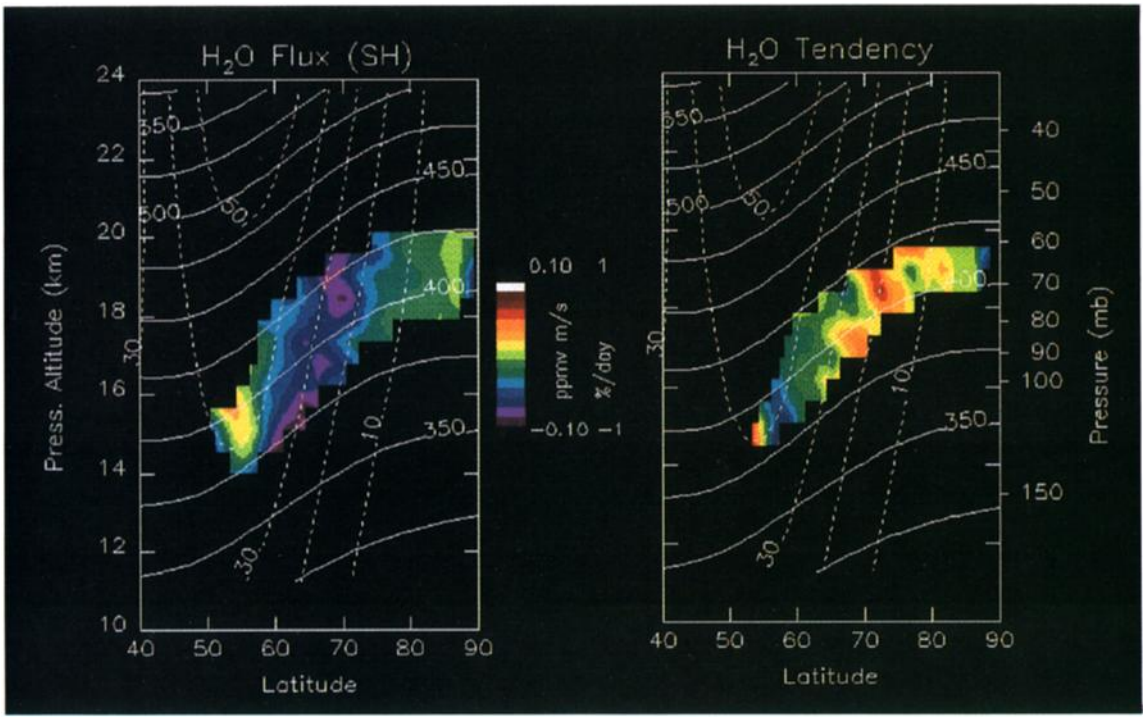

Plate 11. Same as Plate 9, except only for SH H_2O using the reconstructions shown in Plate 4 (right).

signed to span the range of mission radiative transfer environments. Since widespread ice-type PSC formation rarely occurs in the Arctic, the effect of PSCs on the time averaged Arctic heating rates is negligible.

Plate 13 shows the clear-sky zonal mean cooling rates averaged over the two missions. Overlaid are the zonal wind and temperature fields. Generally, smaller cooling rates are associated with colder temperatures, as might be expected, since the polar stratosphere approaches radiative equilibrium during winter [*Fels*, 1985]. The SH vortex is colder, thus the cooling rates are much lower than in the NH vortex. (The model actually calculates slight net heating near 30 mbar.) However, other factors besides temperature can contribute to the cooling rate differences between hemispheres. The severe dehydration within the SH vortex will slightly reduce the overall IR cooling. Ozone destruction will further reduce the spring solar radiative heating.

In order to show the effect of tropospheric clouds and

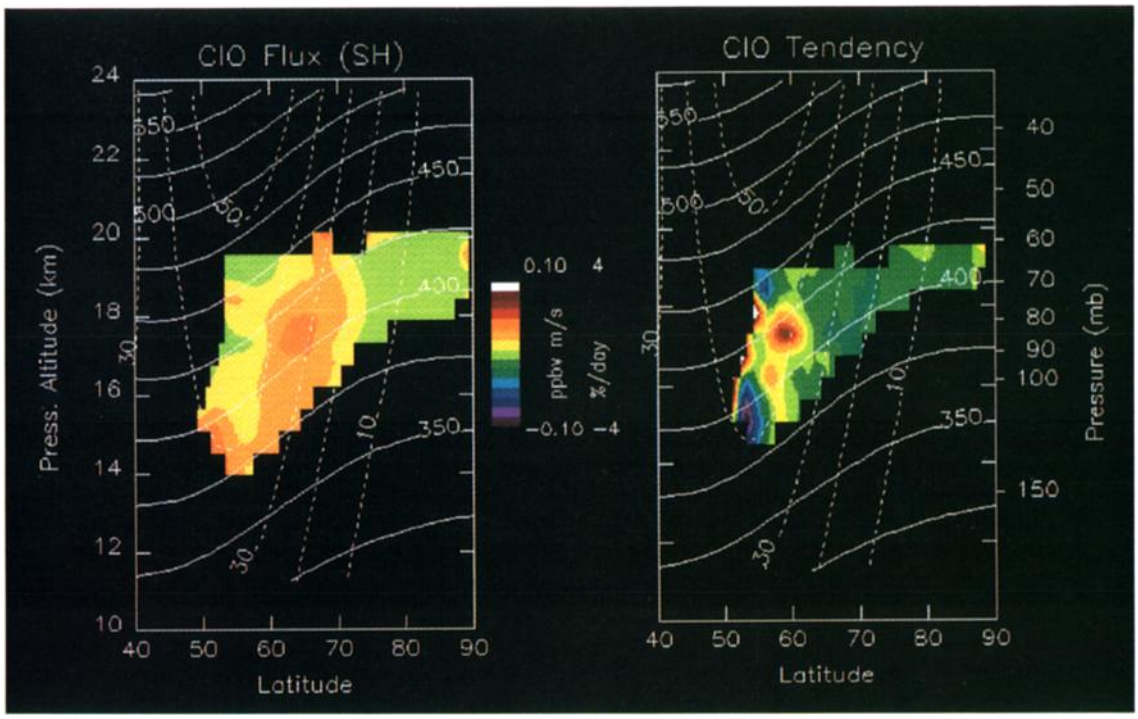

Plate 12. Same as Plate 9, except for SH ClO using the reconstructions shown in Plate 4 (right).

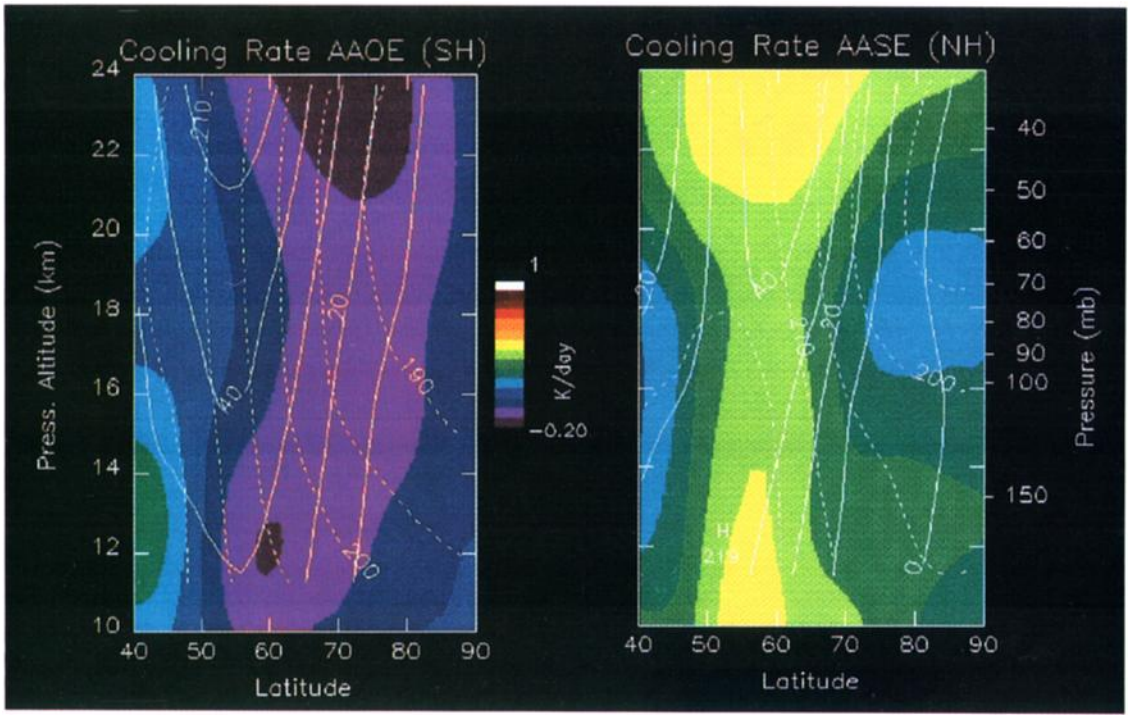

Plate 13. The mission-averaged zonal mean net cooling rates (IR cooling plus solar heating) under clear-sky conditions in deg/d. Zonal wind contours (m/s) (solid) and temperature (K) (dashed) are overlaid.

PSCs on the average radiative cooling rate, Figure 3 shows the computed cooling rate at 50 mbar (~ 20 km) averaged over both mission periods. The cloudy sky cooling rates average about 0.1 K/d larger than the clear-sky rates in both hemispheres. Clouds produce a colder "effective" surface temperature, thereby reducing the upwelling IR flux which heats the polar stratosphere. Even with clouds present, however, the net cooling rates are still small.

Figure 3 shows that when PSCs are present, they act to heat the stratosphere slightly by intercepting more surface

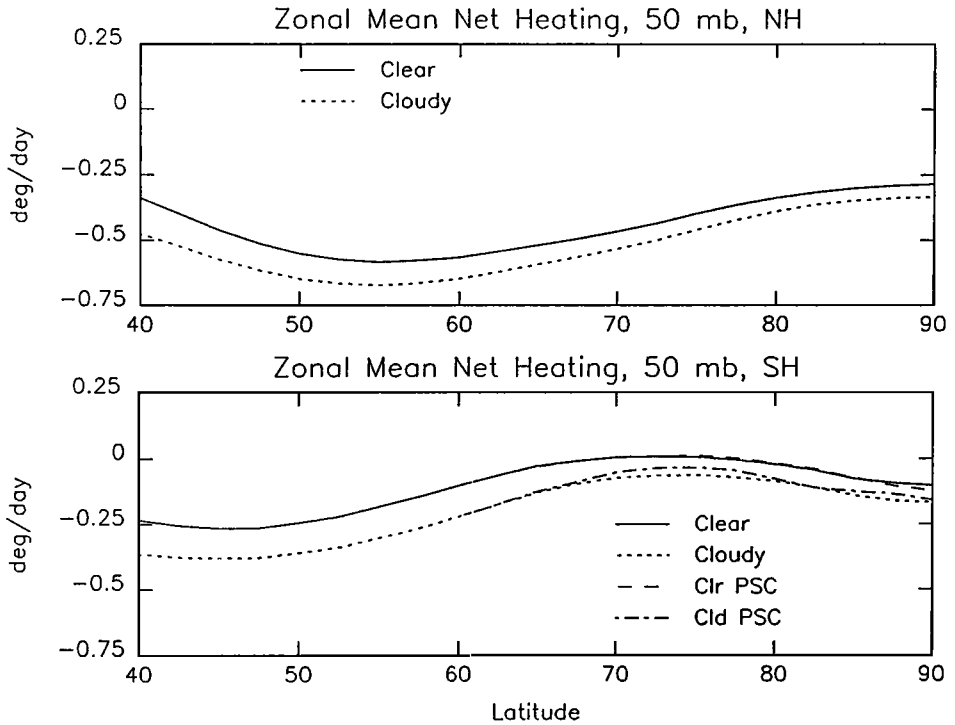

Figure 3. The zonal mean net heating rates at 50 mbar (~20 km) under clear sky conditions (solid line), tropospheric clouds (dotted line), clear-sky with PSCs (dashed line), and tropospheric clouds with PSCs (dot dash line). The general effect of tropospheric clouds is to increase the cooling rates by effectively lowering the surface IR emission temperature, thus cutting off IR heating of the stratosphere. The average effect of PSCs is negligible.

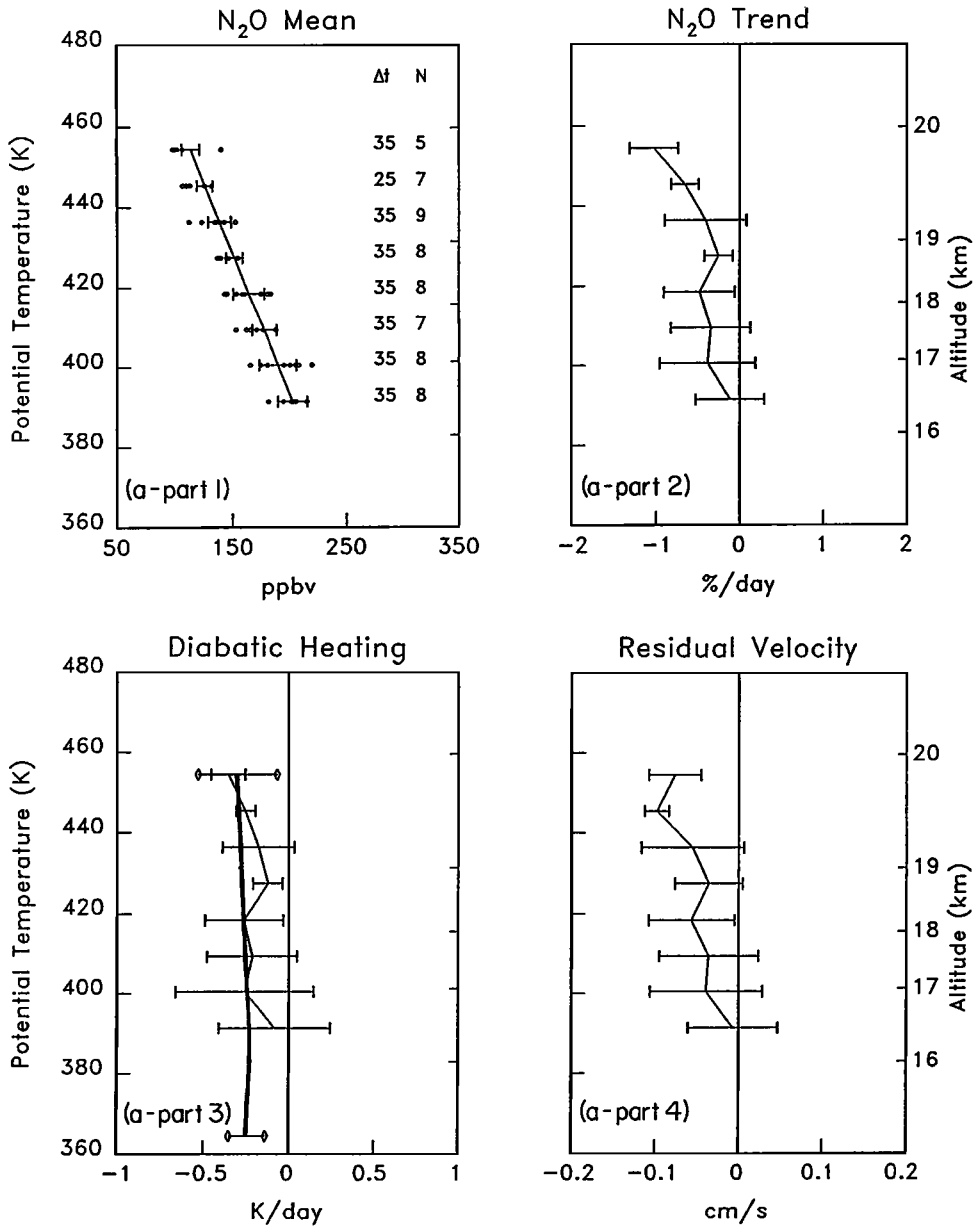

Figure 4. Computation of the cooling rates from N_2O trends using ER-2 profile data as in *Schoeberl et al.* [1990]. (*a*), AASE,(*b*), AAOE. Figures 4*a*, part 1 and 4*b*, part 1; the N_2O mean profile verses potential temperature. All error bars indicate 95% confidence limits. Symbols indicate actual flight data points. Values under the "N" column indicate the number of data points taken at the indicated θ value. Values under the "Δt" column indicate the range of the data in days. Figures 4*a*, part 2 and 4*b*, part 2 show the trend in % per day and confidence limits. Figures 4*a*, part 3 and 4*b*, part 3 show the computed diabatic cooling rate from the N_2O trend (thin line) neglecting the N_2O eddy flux convergence. The heavy line shows the clear-sky cooling rates computed from the radiative transfer model. Uncertainty in the cooling rates due to the variation in dive position and vortex motion is indicated by horizontal bars terminating with diamonds. Figures 4*a*, part 4 and 4*b*, part 4 show the estimated residual vertical velocity computed using the temperature tendency and the N_2O estimated cooling rates assuming $\overline{w}^* = \overline{\theta}_z^{-1}(\overline{Q} - \overline{\theta}_t)$.

IR. Closer to the South Pole, under clear lower sky conditions, PSCs add to the cooling. On the average, however, PSCs do not appear to significantly contribute to the net heating. This result is in agreement with the PSC heating calculations of *Kinne and Toon* [1990].

Validation of Cooling Rates

Schoeberl et al. [1989] estimated the minimum diabatic cooling rate within the Arctic vortex using the ER-2 profile data trends in N_2O. The minimum designation comes from the fact that the diffusive flux of N_2O was neglected. This flux will act to increase N_2O against the tendency for diabatic cooling to decrease N_2O by downward advection. Thus the computed cooling rate from N_2O tendencies could be larger.

Figures 4 shows the estimates of the minimum cooling rate using both Arctic and Antarctic profile data. The 95% confidence limits are also shown. The confidence limits were computed using a 500 case Monte Carlo calculation based upon the observed variance in the data between flights. As discussed by Schoeberl et al. only flight profiles which were

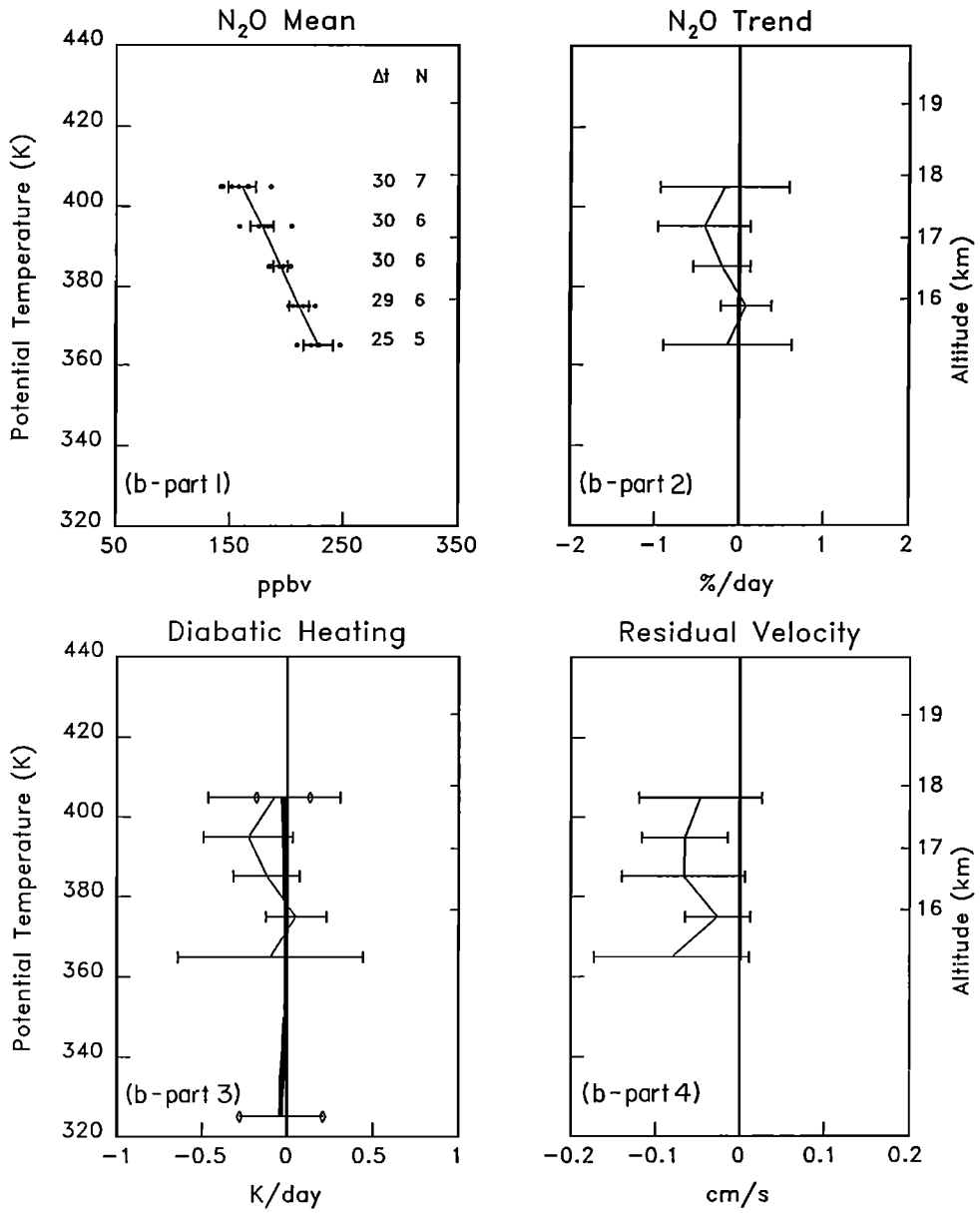

Fig. 4. (continued)

well inside the vortex were used. For AAOE, all flights starting with August 23, 1987 were used except for the flights of September 2 and 9. For AASE, the flights of January 3, 7, 12 and 24, 1989 were not used.

Figures 4 also shows the computed radiative cooling rates for clear-sky conditions with the 95% confidence limits associated with the variation in the ER-2 profile environments; the cloudy sky calculations (not shown, but see Figure 3) have about 0.1K/d greater cooling rates. The computed rates generally fall within the error bars of the N_2O estimates of the minimum cooling rates which increases confidence in the radiative transfer estimates of the cooling. For both AAOE and AASE, the upper limit eddy tendencies for N_2O from Table 3 is ~0.2%/d which would have an insignificant effect on the cooling rate estimates from N_2O and justifies the neglect of this process.

Circulation. Using the clear-sky radiative transfer computations, the residual circulation can be computed (AHL, equation 3.5.2a-e). The residual vertical velocity was calculated using

$$\overline{w}^* = \overline{\theta}_z^{-1}(\overline{Q} - \overline{\theta}_t - \overline{v}^*\overline{\theta}_y) \tag{14}$$

in an iterative fashion, first setting $\overline{v}^*$ to zero; $\overline{v}^*$ is then obtained from the continuity equation,

$$(\cos\phi)^{-1}(\overline{v}^*\cos\phi)_y = -\rho^{-1}(\rho\overline{w}^*)_z \tag{15}$$

and substituted back into (14). Note that $\overline{v}^*$ defined here is the meridional flow along a pressure surface, not an isentrope. The quantitative difference between the two meridional velocities is, however, negligible.

Figure 5 shows the computed vertical velocity overlaid on the zonal mean jet for both hemispheres. The strongest descent is along the jet axis. This is not an unexpected result, considering the structure of the meridional motion field computed in the last section. In the Antarctic, the meridional extent of the vertical velocity field narrows abruptly below 24 km. Above 24 km, eddy activity is greater and extends toward the pole, creating a much broader warm region and hence a broader descent zone [*Mechoso et al.*, 1985].

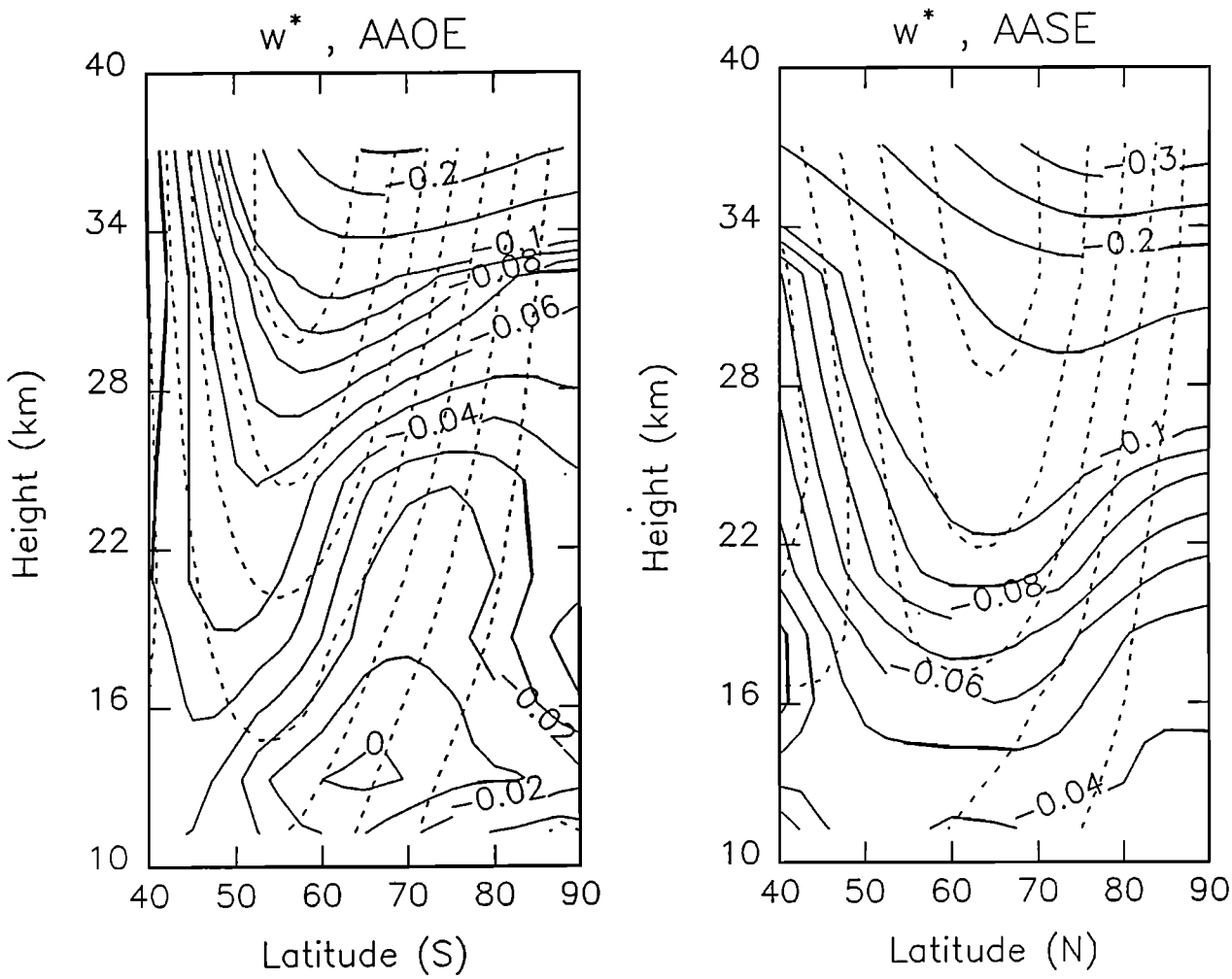

Figure 5. The residual vertical velocity, $\overline{w}^*$, in cm/s estimated from the cooling rates shown in Plate 13. Overlaid are the zonal mean winds (dotted lines) in m/s.

The residual vertical velocity in the Arctic has a comparatively broader latitudinal width and is generally stronger in the lower stratosphere. This result is consistent with the estimates of the vertical motion from the ER-2 profile data (Figure 4) and from aerosol observations [*Kent et al.*, 1985].

Figure 6 shows a cross section of the meridional flow (shown as v) at 50 mbar computed from the diabatic cooling rates, (14 and 15), and the meridional flow, $\overline{v}^*$, computed using the trajectory estimates of D (5). Also shown for reference is the zonal mean wind and $\overline{D}$. The magnitude and structure of the two computed meridional velocity fields are in remarkable agreement in both hemispheres. Aside from the small (0.03 m/s) offset between the non steady state, diabatically computed value of $\overline{v}^*$ and the steady state, trajectory estimate in the SH vortex, the general agreement in the two $\overline{v}^*$ values is an important result, considering the independence of the methods used to derive them. The result suggests overall consistency in the picture of the vortex circulation, and a correct quantitative assessment of the magnitude of the circulation.

Summary and Discussion

In the previous sections, the AAOE and AASE aircraft campaign observations have been used to produce a basic picture of the lower stratospheric polar vortex structure as it appeared during the two missions. This picture (Figure 7), which is common to both the NH and SH vortices, contains the following elements:

1. Reconstructed aircraft data shows that there is a sharp meridional N_2O gradient roughly located at the latitude of the polar night jet core and co-located with a similar gradient in potential vorticity. N_2O isopleths within the polar vortex are displaced downward 2-3 km relative to the vortex exterior.

2. At 50 mbar poleward zonal mean meridional flow of ~0.1 m/s exists on the anticyclonic side of the polar night jet and persists up to the core of the jet. Much smaller zonal mean meridional poleward flow exists on the cyclonic side of the jet (~0.03 to 0 m/s).

3. Zonal mean, diabatic descent associated with the vortex is coincident with the jet core. The magnitude of this descent increases with altitude. At 20 km (~ 50 mbar), the descent rate is about 0.04 cm/s for the Antarctic (AAOE) compared to 0.08 cm/s for the Arctic (AASE). This corresponds to a dynamical heating rate of 0.25 to 0.5 deg/d, respectively. The descent rate on the cyclonic side of both SH and NH vortices is small, consistent with their near radiative equilibrium temperatures.

4. On the anticyclonic side of the vortex, the eddy mixing rate during this low wave activity period is computed to be 2.0×10^5 m^2/s. Moving poleward, the diffusion rates then drop off by about an order of magnitude or more at the jet core, increasing slightly towards the vortex interior.

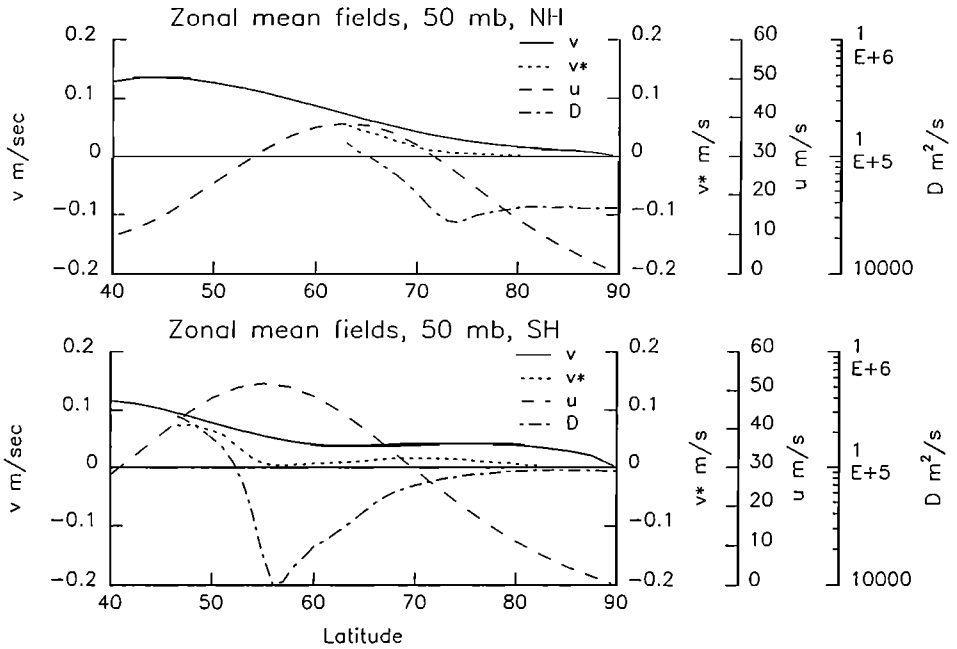

Figure 6. Zonal mean fields at 50 mbar as in Figure 3. Solid line shows the value of $\overline{v}^*$ computed from the diabatic cooling rates (labeled v in the figure) in m/s. Dotted line shows $\overline{v}^*$ computed using trajectory estimates of D. Also shown are the computed values of D (dash-dot) in m^2/s and $\overline{u}$ (dashed line) in m/s.

Somewhat higher diffusion rates are evident below the SH vortex 400K surface.

The circulation system described above was derived using a trajectory model to calculate diffusion rates, and a radiative transfer model to compute cooling rates. The two independent computations produce a consistent meridional circulation which lends confidence to the results. The existence of low mixing rates within the vortex also appears to be consistent with the observation of steep meridional gradients in N_2O, O_3, H_2O, NO_y, and ClO. The picture that emerges is that the polar vortex is not that of a "flowing processor" as argued by *Proffitt et al.* [1990], but a region of highly isolated air as argued by *Hartmann et al.* [1989].

The polar vortex, as an entity, is shaped by the action of mid-latitude planetary waves. Exchange between polar vortex and mid-latitude air during the mission periods appears to be confined to the vortex edge. This exchange is basically a one-way transport; vortex material is stripped away to mid-latitudes as the vortex erodes. The latitude variation of the eddy mixing then contributes to the trace gas "edge" formation along with the differential vertical advection of tracers. Within the vortex, little mixing or transport of long-lived tracers takes place. This picture of the vortex is in broad agreement with barotropic numerical model simulations [*Juckes and McIntyre*, 1987],three dimensional model simulations [*Mahlman and Umscheid*, 1987], and the assimilated data transport studies of *Rood et al.* [this issue].

The smaller area covered by the NH vortex compared to its SH counterpart is likely due to the greater level of planetary wave activity in the NH which erodes the vortex more rapidly. Despite these interhemispheric differences in wave activity, the similarity in long-lived tracer distributions is probably rooted in the tendency for the effects of eddy mixing and the secondary circulation on long-lived tracer distributions to cancel (11).

Since the SH vortex jet core is located at lower latitudes, the dynamical heating associated with the jet core descent zone is further from the pole. Thus the SH, polar, lower stratosphere can approach radiative equilibrium temperatures, which are cold enough to support widespread PSC activity. The interhemispheric differences in the reconstructed O_3, ClO, H_2O, and NO_y distributions appear mainly to be due to PSC processes which produce wide areas of dehydration, denitrification, elevated ClO amounts, and O_3 loss. Thus the chemical differences between the SH and NH winter stratospheres are ultimately arise from in the interhemispheric differences in planetary wave activity.

Estimates of the fluxes of constituents within the SH vortex are given in Table 3. These estimates are made using the flux-gradient relation and the diffusion coefficients derived from ensemble trajectory computations. As mentioned above, flux convergences are largest at or near the vortex edge. For long-lived tracers, the diffusive eddy flux convergence was computed to be about 0.2%/d. Interior to the vortex, flux convergences are very small. This latter result has important implications for both water vapor and ozone inside the SH vortex. For water, it suggests that the dehydration of air in the outer SH vortex region at 55-65S is probably not due to the mixing of air from the more severely dehydrated poleward region. An alternative explanation is that PSC dehydration has occurred, perhaps intermittently in the 55-65S region as well. This hypothesis appears consistent with meteorological observations. For ozone, the low computed eddy flux convergences suggest that chemical processes dominate the ozone budget; dynamical transport can be all but neglected, in agreement with the analysis of *Hartmann et al.* [1989].

Tuck et al. [this issue] argues that material is being transferred from the vortex edge to mid-latitudes much more rapidly than suggested by the calculations presented here. A rapid transfer of high ClO air from within the vortex to mid-latitudes might explain the high mid-latitude ClO measurements reported by *Toohey et al.* [1991]. However, since the vortex area does not noticeably change during the mission periods, high PV air eroded from the vortex edge would have to be replaced by high PV air descending from higher altitudes. This, in turn, suggests much higher diabatic cooling rates. Neither the N_2O trend measurements nor the radiative transfer computations reported here appear to be consistent with that requirement. Furthermore, *Mather and*

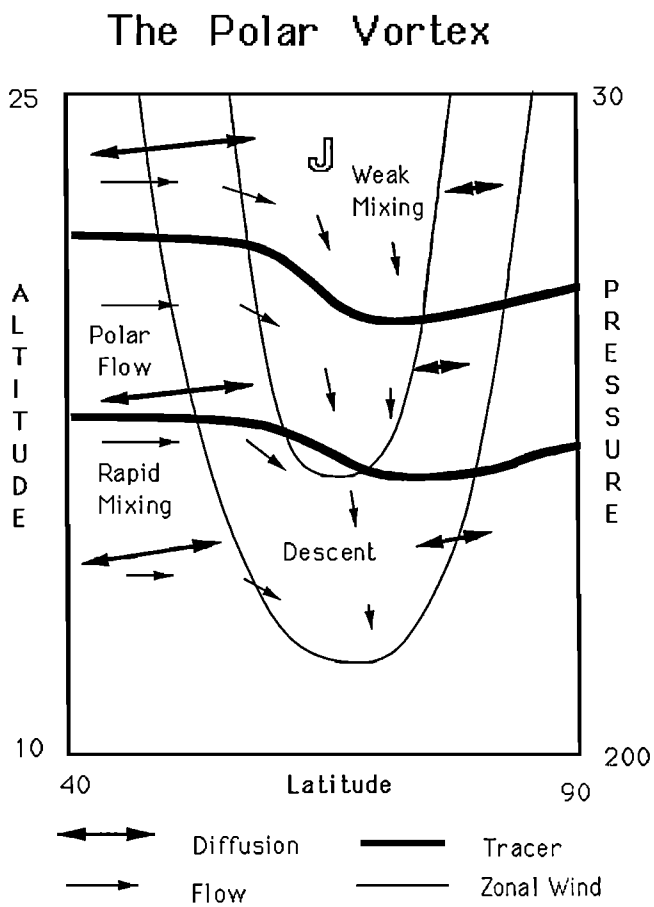

Figure 7. A schematic diagram of the circulation and mixing associated with the "generic" polar vortex. Double arrows indicate mixing with longer arrows representing larger mixing rates. Single arrows indicate flow directions, length approximately indicating magnitude. Thin lines show zonal wind contours; J indicates jet core. Long-lived tracer isopleths are shown by thick line. This picture of the polar vortex is relevant to the Arctic mid-winter period or the early spring Antarctic period. Approximate altitudes and pressures in mbar are given along the ordinate.

Brune [1990] and D. B. Considine et al. (Heterogeneous conversion of N_2O_5 to HNO_3 on background stratospheric aerosols: Comparisons of model results with data, submitted to *Geophysical Research Letters*, 1991) have shown that heterogenous chemistry on background sulphate aerosols have the potential for producing high mid-latitude ClO amounts in agreement with the aircraft measured values.

Finally, one question unanswered by these studies is: Why should the eddy diffusion rate decrease so rapidly across the vortex boundary? It is clear that the formation of tight PV gradients at the vortex boundary is related to the planetary wave breaking phenomena at the vortex edge. The low level of wave activity within the vortex may be related to the exclusion of planetary waves from that region by the strong winds. Planetary wave propagation studies by *Karoly and Hoskins* [1982] and *Palmer* [1982] suggest that planetary waves tend to propagate away from the vortex edge. This seems to be the climatological rule as indicated by the transient and stationary Eliassen Palm flux computations given by *Randel* [1987]. Thus the exclusion of planetary waves from the vortex may become more effective as the vortex edge develops.

Appendix: The N_2O Coordinate

Since N_2O is a conserved tracer, it can be used as a coordinate [*Schoeberl et al.*, 1989]. To illustrate this point more precisely, the thermodynamic equation can be written in the Lagrangian form:

$$\frac{d\theta}{dt} = Q \tag{16}$$

where Q is, by definition, the net diabatic heating rate and θ is potential temperature. Now let N_2O be the "vertical" coordinate N, with the "vertical velocity" $\dot{N}$. In the Eulerian form, the above becomes

$$\theta_t + v^n\theta_y + u^n\theta_x + \dot{N}\theta_N = Q \tag{17}$$

Equation (17) thus describes the thermodynamic situation along an N_2O contour, v^n is the N-S velocity along the N_2O isopleth, u^n is the E-W velocity. Subscripts denote partial differentiation. Since N_2O is conserved, $\dot{N} = 0$. Taking each variable as a zonal mean, denoted with an overbar, plus a deviation whose zonal mean is zero, denoted by a prime, then zonally averaging the result,

$$\bar{\theta}_t + \overline{u'\theta'_x} + \overline{v'\theta'_y} + \bar{v}\bar{\theta}_y = \bar{Q} \tag{18}$$

where the n superscript has been dropped. The four terms on the left hand side of (18) are the thermal tendency, two components of the eddy heat transport, and the mean heat transport, respectively. *Proffitt et al.* [1990] argues that the transport velocity can be computed simply using the diabatic cooling rate and the mean meridional isentropic

gradient, $\bar{\theta}_y$, along the average N_2O contour. Essentially, this amounts to simplifying (18) to

$$\bar{v} = \bar{Q}/\bar{\theta}_y. \quad (19)$$

Clearly, this approximation neglects the tendency term and the eddy heat transport; the latter is usually a significant component of the transport circulation in Eulerian coordinates [*Andrews et al.*, 1987]. If (19) is used along the 220 ppb N_2O contour along with the cooling rates shown in Plate 13, a meridional velocity of 1.6 m/s is obtained between 55 and 60N. This implies an extreme zonal deceleration of nearly 10 m/s/d. Clearly, the eddy heat flux must balance most of the radiative cooling, and the *Proffitt et al.* [1990] circulation is, at best, an upper bound on the magnitude of the meridional transport velocity.

Acknowledgments. The authors are grateful to the number of people who have contributed to making the polar aircraft missions a success. They include Adrian Tuck, project scientist; Estelle Condon, project manager; the intrepid ER-2 pilots; the experimentalists whose data were used in this paper: Max Loewenstein and Jim Podolske, N_2O; Jim Anderson and Bill Brune, ClO; Dave Fahey, NO_y; Mike Proffitt, O_3; Ken Kelly, H_2O; K. R. Chan, meteorological measurements; the NMC CAC group: Ron Nagatani and Jim Miller; the theorists who contributed comments and helpful suggestions: Julio Bacmeister, Dennis Hartmann, Michael McIntyre, Steve Wofsy, Alan Plumb; and, finally, the NASA Ames support team, who made the mission possible.

REFERENCES

Anderson, J. G., et al., Kinetics of O_3 destruction by ClO and BrO within the Antarctic vortex: An analysis based upon in situ ER-2 data, *J. Geophys. Res., 94*, 11480-11520, 1989.

Andrews, D. G., J. R. Holton and C. B. Leovy, *Middle Atmosphere Dynamics*, 489 pp., Academic Press, San Diego, Calf., 1987.

Austin, J., and A. F. Tuck, The calculation of stratospheric air parcel trajectories using satellite data, *Q. J. R. Meteorol. Soc., 111*, 279-307, 1985.

Browell, E. V., et al., Airborne lidar observations in the wintertime Arctic stratosphere: Ozone, *Geophys. Res. Lett., 17*, 325-328, 1990.

Brune, B., D. W. Toohey, J. G. Anderson, and K. R. Chan, In situ observations of CLO in the Arctic stratosphere: ER-2 aircraft results from 59°N to 80°N latitude, *Geophys. Res. Lett., 17*, 505-508, 1990.

Butchart, N., and E. Remsberg, The area of the stratospheric polar vortex as a diagnostic for tracer transport on an isentropic surface, *J. Atmos. Sci, 43*, 1319-1339, 1986.

Fahey, D. W., et al., Observations of denitrification and dehydration in the winter polar stratosphere, *Nature, 344*, 321-324, 1990*a*.

Fahey, D. W., et al., A diagnostic for denitrification in the winter polar stratosphere, *Nature, 344*, 698-702, 1990*b*.

Fels, S. B., Radiative–dynamical interactions in the middle atmosphere, *Adv. Geophys., 28A*, 277-300, 1985.

Fritts, D. C., Gravity wave saturation in the middle atmosphere: A review of theory and observations, *Rev. Geophys., 22*, 275-308, 1984.

Galimore, R. G. and D. R. Johnson, The forcing of the meridional circulation of the isentropic zonally average circumpolar vortex, *J. Atmos. Sci., 38*, 583-599, 1981.

Gandrud, B. W., et al., The January 30, 1989 Arctic polar stratospheric clouds (PSC) event: Evidence for a mechanism of dehydration, *Geophys. Res. Lett., 17*, 457-460, 1990.

Hartmann, D., et al., Transport into the South Polar vortex in early spring, *J. Geophys. Res., 94*, 16, 779-16,796, 1989.

Haynes, P. H., et al., On the downward control of extratropical diabatic circulations by eddy-induced mean zonal forces. *J. Atmos. Sci., 47*, 651-678, 1991.

Holton, J. R., Wave propagation and transport in the middle atmosphere, *Philos. Trans. R. Soc. London, Sec. A, 296*, 73-85, 1980.

Holton, J. R., A dynamically based transport parameterization for one-dimensional photochemical models of the stratosphere, *J. Geophys Res., 91*, 2681-2686, 1986.

Juckes, M. N., and M. E. McIntyre, A high resolution, one layer model of breaking planetary waves in the stratosphere, *Nature, 328*, 590-596, 1987.

Karoly, D. J., and B. Hoskins, Three dimensional propagation of planetary waves, *J. Meteorol. Soc. Jpn., 61*, 510-523, 1982.

Kawa, S. R., et al., Photochemical partitioning of the reactive nitrogen and chlorine reservoirs in the high latitude stratosphere, *J. Geophys. Res.*, this issue.

Kelly, K. K., et al., Dehydration in the lower Antarctic stratosphere during late winter and early spring, 1987, *J. Geophys. Res., 94*, 11,317-11,357, 1989.

Kent, G. S., C. R. Trepte, U. O. Farrukh, and M. P. McCormick. Variation in the stratospheric aerosol associated with the north cyclonic polar vortex as measured by the SAM II satellite sensor, *J. Atmos. Sci., 42*, 1536 - 1551, 1985.

Kida, H., General circulation of air parcels and transport characteristics derived from a hemispheric GCM, Part 2, Very long term motions of air parcels in the troposphere and stratosphere, *J. Meteorol. Soc. Jpn., 61*, 510-523, 1983.

Kinne, S., and O. B. Toon, Radiative effects of polar stratospheric clouds, *Geophys. Res. Lett., 17*, 373-376, 1990.

Lait, L. R., et al., Reconstruction of O_3 and N_2O fields from the ER-2, DC-8 and balloon observations, *Geophys. Res. Lett., 17*, 521-524, 1990.

Loewenstein, M., J. R. Podolske, K. R. Chan, and S. E. Strahan, Nitrous oxide as a dynamical tracer in the 1987 Airborne Antarctic Ozone Experiment, *J. Geophys. Res., 94*, 11,589-11,598, 1989.

Loewenstein, M., J. R. Podolske, K. R. Chan and S. E. Strahan, N_2O as a dynamical tracer in the arctic vortex, *Geophys. Res. Lett., 17*, 477-480, 1990.

Mahlman, J. D., and L. J. Umscheid, Comprehensive modeling of the middle atmosphere: The influence of horizontal resolution, in *Transport Processes in the Middle Atmosphere*, edited by G. Visconti and R. Garcia, D. Reidel, pp. 251-266, Hingham, Mass., 1987.

Mahlman, J. D., H. Levy II, and W. J. Moxim, Three dimensional simulations for stratospheric N_2O: Predictions for other trace constituents, *J. Geophys. Res., 91*, 2687-2708, 1986.

Mather, J. H., and W. H. Brune, Heterogeneous chemistry on liquid sulfate aerosols: A comparison of in situ measurements with zero-dimensional model calculations, *Geophys. Res. Lett., 17*, 1283-1286, 1990.

McCormick, M. P., C. R. Trepte, and M. C. Pitts, Persistence of polar stratospheric clouds in the southern polar region, *J. Geophys. Res., 94*, 11,241-11,253, 1989.

Mechoso, C. R., D. L. Hartmann, and J. D. Farrarra, Climatology and interannual variability of wave, mean-flow interaction in the southern hemisphere, *J. Atmos. Sci., 42*, 2189-2206, 1985.

Murphy, D. M., Local ozone loss rates calculated along ER-2 flight tracks, *J. Geophys.*, in press, 1991.

Nagatani, R. M., A. J. Miller, M. E. Gelman, and P. A. Newman, A comparison of Arctic lower stratospheric winter temperatures for 1988-1989 with temperatures since 1964, *Geophys. Res. Lett., 17*, 333-336, 1990.

Newman, P. A., M. R. Schoeberl, R. A. Plumb, and J. E. Rosenfield, Mixing rates calculated from potential vorticity, *J. Geophys Res., 93*, 5221-5240, 1988*a*.

Newman, P. A., et al., Meteorological atlas of the Southern Hemisphere lower stratosphere for August and September 1987, *NASA Tech. Memo, 4049*, 131 pp., 1988*b*.

Newman, P. A., et al., Meteorological atlas of the Northern Hemisphere lower stratosphere for January and February 1989

during the Airborne Arctic Stratospheric Expedition, *NASA Tech. Memo, 4145*, 185 pp., 1989.

Palmer, T. N., Properties of Eliassen–Palm flux for planetary scale motions, *J. Atmos. Sci., 39*, 992-997, 1982.

Plumb, R. A., Ozone depletion in the Arctic, *Nature, 347*, 20-21, 1990.

Plumb, R. A., and J. D. Mahlman, The zonally- averaged transport characteristics of the GFDL general circulation/transport model, *J. Atmos. Sci., 44*, 298-327, 1987.

Prather, M., and A. Jaffe, Global impact of the Antarctic ozone hole: Chemical propagation, *J. Geophys. Res., 95*, 3473-3492, 1990.

Proffitt, M. H., et al., Evidence for diabatic cooling and poleward transport within and around the 1987 Antarctic ozone hole, *J. Geophys. Res., 94*, 16,797-16,7814, 1989*a*.

Proffitt, M. H., et al., High-latitude ozone loss outside the Antarctic ozone hole, *Nature, 342*, 233-237, 1989*b*.

Proffitt, M. H., et al., A chemical definition of the boundary of the Antarctic ozone hole, *J. Geophys. Res., 94*, 11,437-11,448, 1989*c*.

Proffitt, M. H., et al., Ozone loss in the Arctic polar vortex inferred from high-altitude aircraft measurements, *Nature, 347*, 31-36, 1990.

Randel, W. J., Global atmospheric circulation statistics, 1000–1 mbar, NCAR/TN-295+STR, 245 pp, 1987.

Remsberg, E. E., et al., Implications of the stratospheric water vapor distribution as determined from the Nimbus 7 LIMS experiment, *J. Atmos. Sci., 41*, 2934-2945, 1984.

Rood, R. B., et al., Stratospheric temperatures during AASE: Results from STRATAN *Geophys. Res. Lett., 17*, 337-340, 1990.

Rood, R. B., et al., Episodic total ozone minima and associated effects on heterogeneous chemistry and lower stratospheric transport, *J. Geophys. Res.*, this issue.

Rosenfield, J. E., A simple parameterization of ozone infrared absorption for atmospheric heating rate calculations, *J. Geophys. Res., 96*, 9065-9074, 1991.

Rosenfield, J. E., Radiative effects of polar stratospheric clouds during Airborne Arctic Ozone Experiment and Airborne Arctic Stratospheric Expedition, *J. Geophys. Res.*, this issue.

Rosenfield, J. E., M. R. Schoeberl, P. A. Newman and L. R. Lait, Radiative heating rates during the Airborne Arctic Stratospheric Expedition, *Geophys. Res. Lett., 17*, 349-352, 1989.

Rosenfield, J. E., M. R. Schoeberl, and M. A. Geller, A computation of the stratospheric diabatic circulation using an accurate radiative transfer model, *J. Atmos. Sci., 44*, 859-876, 1987.

Salby, M. L., et al., Global transport calculations with an equivalent barotropic system, *J. Atmos. Sci., 47*, 188-214, 1990.

Schoeberl, M. R., and D. L. Hartmann, The dynamics of the stratospheric polar vortex and its relation to the springtime ozone depletions, *Science, 251*, 46-52, 1991.

Schoeberl, M. R., and L. R. Lait, Conservative coordinate transformations for atmospheric measurements, in *EOS NATO Summer School*, edited by G. Visconti and J. Gille, in press, 1991.

Schoeberl, M. R., et al., Stratospheric constituent trends from ER-2 profile data, *Geophys. Res. Lett., 17*, 469-472, 1990.

Schoeberl, M. R., et al., Reconstruction of the constituent distribution and trends in the Antarctic polar vortex from ER-2 flight observations, *J. Geophys. Res., 94*, 16815-16845, 1989.

Solomon, S., Progress towards a quantitative understanding of Antarctic ozone depletion, *Nature, 347*, 347-354, 1990.

Telegadas, K., The relationship between stratospheric circulation patterns and radioactive debris in early 1963. *J. Appl. Meteorol., 6*, 137-141, 1967.

Toohey, D. W., et al., In situ measurements of mid-latitude ClO in winter, *Geophys. Res. Lett., 18*, 21-24, 1991.

Toon, G. C., et al., Infrared aircraft measurements of stratospheric composition over Antarctica during September, *J. Geophys. Res., 94*, 16,571-16,596, 1989.

Tuck, A. F., Synoptic and chemical evolution of the Antarctic vortex in late winter and early spring, 1987, *J. Geophys. Res., 94*, 11,687-11,737, 1989.

Tuck, A. F. et al., The planning and execution of ER-2 and DC-8 aircraft flights over Antarctica, August and September 1987, *J. Geophys. Res., 94*, 11,181-11,222, 1989.

Tuck, A. F. et al., Polar Stratospheric Cloud-processed air and potential vorticity in the northern hemisphere lower stratosphere at mid-latitudes during winter, *J. Geophys. Res.*, this issue, 1991.

Tung, K. K., On the two dimensional transport of trace gases in isentropic coordinates, *J. Atmos. Sci., 39*, 2330-2355, 1982.

Tung, K. K., A coupled model of zonally averaged dynamics, radiation and chemistry, *Transport Processes in the Middle Atmosphere*, pp. 183-198, edited by G. Visconti and R. Garcia, D. Reidel, Hingham, Mass., 1987.

Turco Turco, R., R. A. Plumb, and E. Condon, The Airborne Arctic Stratospheric Expedition: Prologue, *Geophys. Res. Lett., 17*, 313-316, 1990.

Wofsy, S. C., et al., Nucleation and growth of $HNO_3 3H_2O$ particles in the polar stratosphere, *J. Atmos. Sci., 47*, 2004-2012, 1990.

Yang, H., K. K. Tung, and E. Olaguer, Nongeostrophic theory of zonally averaged circulation, Part II, Elliassen–Palm flux divergence and isentropic mixing coefficient, *J. Atmos. Sci., 47*, 215-241, 1990.

L. Lait, P. Newman, J. Rosenfield, and M. Schoeberl, Code 916, NASA Goddard Space Flight Center, Greenbelt, MD 20771.

(Received February 14, 1991;
revised August 14, 1991;
accepted August 16, 1991)